

Entanglement-enhanced learning of quantum processes at scale

Alireza Seif,^{1,*} Senrui Chen,^{2,*} Swarnadeep Majumder,¹ Haoran Liao,³ Derek S. Wang,¹
Moein Malekakhlagh,¹ Ali Javadi-Abhari,¹ Liang Jiang,² and Zlatko K. Mineev¹

¹*IBM Quantum, IBM T.J. Watson Research Center, Yorktown Heights, NY, USA*

²*Pritzker School of Molecular Engineering, University of Chicago, Chicago, IL, USA*

³*Department of Physics, University of California, Berkeley, CA 94720, USA*

Learning unknown processes affecting a quantum system reveals underlying physical mechanisms and enables suppression, mitigation, and correction of unwanted effects. Describing a general quantum process requires an exponentially large number of parameters. Measuring these parameters, when they are encoded in incompatible observables, is constrained by the uncertainty principle and requires exponentially many measurements. However, for Pauli channels, having access to an ideal quantum memory and entangling operations allows encoding parameters in commuting observables, thereby exponentially reducing measurement complexity. In practice, though, quantum memory and entangling operations are always noisy and introduce errors, making the advantage of using noisy quantum memory unclear. To address these challenges we introduce error-mitigated entanglement-enhanced learning and show, both theoretically and experimentally, that even with noise, there is a separation in efficiency between learning Pauli channels with and without entanglement with noisy quantum memory. We demonstrate our protocol’s efficacy in examples including hypothesis testing with up to 64 qubits and learning inherent noise processes in a layer of parallel gates using up to 16 qubits on a superconducting quantum processor. Our protocol provides accurate and practical information about the process, with an overhead factor of 1.33 ± 0.05 per qubit, much smaller than the fundamental lower bound of 2 without entanglement with quantum memory. Our study demonstrates that entanglement with auxiliary noisy quantum memory combined with error mitigation considerably enhances the learning of quantum processes.

I. INTRODUCTION

Understanding and characterizing unknown quantum processes are crucial for advancing physics and developing engineered quantum systems. A detailed knowledge of noise processes enables quantum computers to perform useful tasks with the help of quantum error mitigation [1–3] in the near-term and through quantum error correction in the future [4]. Describing a general quantum process becomes increasingly complex as the system size grows, due to the exponential growth of Hilbert space. To learn the parameters describing a process, one measures the physical observables that encode them. However, these observables often do not commute, and due to the constraints imposed by the uncertainty principle, learning them requires an exponentially large number of measurements.

Counterintuitively, entanglement, which is one of the main factors in increasing complexity, can enhance our ability to learn properties of physical systems if used cleverly. For example, entangling quantum sensors provides a quadratic advantage in their sensitivity [5, 6]. Entangled measurements in

quantum tomography can reduce its cost to a degree [7–10]. Recently, it has been shown that entanglement with quantum memory can in theory provide exponential advantage in learning quantum processes [11–15]. However, in practice, one might suspect that adding even more fragile entanglement and unavoidably-faulty auxiliary components to an already noisy system should limit the entanglement-based advantage [16–18]. In some classification and hypothesis testing tasks, this advantage can partially survive in experiments [14]. But beyond simple proofs of principle, can this advantage be observed in practical real-world experiments?

Here, we demonstrate that the advantage of using entanglement with quantum memory for learning physical processes can persist even in the presence of noise. This is achieved by designing a protocol that efficiently mitigates errors in the noisy auxiliary quantum memory (see Fig. 1). Specifically, we focus on the practical case of learning Pauli channels without any assumptions about their structure. Pauli channels are now routinely used in state-of-the-art benchmarking [19, 20], error mitigation [1–3, 21], and error correction [22, 23] applications. Moreover, in the ideal scenario, there are rigorous guarantees of exponential separation between learning with and without quantum memory for Pauli channels [12, 24–26]. We show, both theoretically

* These authors contributed equally to this work.

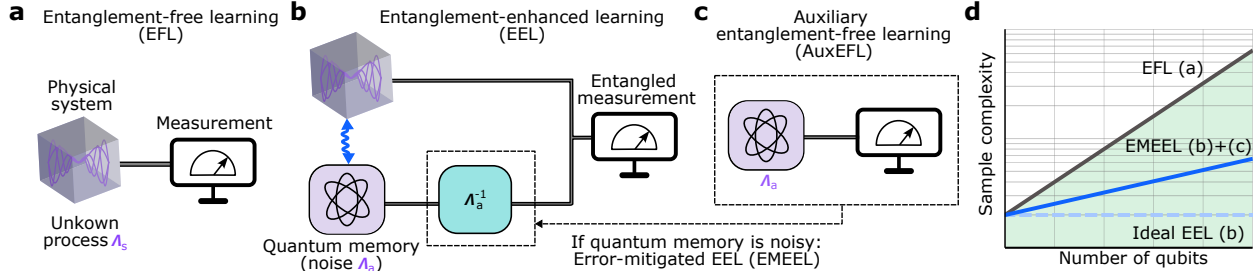


FIG. 1. **Different scenarios for learning an unknown quantum process.** **a**, Entanglement-free learning (EFL) with the direct measurement of the process Λ_s (a Pauli channel in this work). **b**, Entanglement-enhanced learning (EEL) using a quantum memory. This strategy, through entanglement with an ideal noiseless quantum memory, provides an exponential advantage in the number of samples required for learning Λ_s . In practice, quantum memory can be noisy (affected by another unknown process Λ_a). **c**, Noise on quantum memory, Λ_a , can be learned efficiently using direct entanglement-free learning on auxiliary qubits (AuxEFL). This noise can be simplified to a generalized depolarization channel, making AuxEFL considerably simpler and more efficient than EFL. We can then apply error mitigation in panel (b) and apply Λ_a^{-1} to recover correct results with possibly an exponential overhead using error-mitigated EEL (EMEEL). **d**, The sample complexity of EFL scales exponentially, whereas that of EEL remains independent of system size. Although EMEEL also has exponential sample complexity, it can break EFL’s fundamental lower bound and achieve better scaling by leveraging entanglement with quantum memory and error mitigation, provided the noise on the quantum memory is weak.

and experimentally, that despite the generally exponential overhead from error mitigation, our protocol not only rigorously improves the sample complexity of learning but also breaks the fundamental limit on the number of learning samples needed without access to entanglement with a quantum memory.

II. LEARNING PAULI CHANNELS WITH AND WITHOUT QUANTUM MEMORY

Pauli channels are crucial in quantum information processing because they provide a practically relevant model for errors in quantum computers [27, 28]. Physically, Pauli channels describe a probabilistic mixture of Pauli operations. Their practical relevance is further motivated by the fact that arbitrary quantum channels can be transformed into Pauli channels through Pauli twirling, which involves averaging over the application of random Pauli gates before and after the channel [29–31].

A Pauli channel \mathcal{E} on n qubits can be fully specified by its 2^n Pauli fidelities λ_k corresponding to Pauli operator P_k , i.e., $\mathcal{E}(\rho) = \sum_k \lambda_k P_k \text{Tr}(\rho P_k)/4^n$. These fidelities can be learned by preparing and measuring a quantum system in different bases [28]. However, it has been shown recently that such a scheme requires $\Omega(2^n/\varepsilon^2)$ measurements to estimate every λ_k to $\pm\varepsilon$ precision with high probability [24, 25]. This lower bound holds even if one is allowed to concatenate arbitrarily many copies of

the Pauli channel and control operations before doing one measurement. We refer to this general class of protocols that only utilize the qubits directly affected by the channel as entanglement-free learning (EFL), see Fig. 1a. Note that with this terminology we still allow for entangling operations acting on the system alone, but exclude entanglement between system and auxiliary memory qubits.

Access to quantum memory, however, significantly alters the resource requirements. Specifically, we entangle each system qubit with an auxiliary qubit in the Bell basis, i.e., $|\Phi_1\rangle = 1/\sqrt{2}(|00\rangle + |11\rangle)$. The state of n such pairs is then given by $|\Phi_n\rangle = 2^{-n/2} \sum_{i=0}^{2^n-1} |ii\rangle$, where the first and second index correspond to the 2^n computational basis states of n system and auxiliary qubits, respectively. Applying the Pauli channel \mathcal{E} to the system and the identity channel \mathcal{I} to the auxiliary qubits prepares

$$(\mathcal{E} \otimes \mathcal{I})(|\Phi_n\rangle\langle\Phi_n|) = \sum_k \lambda_k P_k \otimes P_k^\top / 4^n, \quad (1)$$

which is also known as the Choi state of the channel [32]. We then observe that we can measure all $P_k \otimes P_k^\top$ simultaneously and obtain the corresponding λ_k as they commute, i.e., $[P_k \otimes P_k^\top, P_j \otimes P_j^\top] = 0$ for all P_k, P_j . This can be done via the Bell basis measurement, akin to a multi-qubit version of superdense coding [33]. We refer to this scheme as entanglement-enhanced learning (EEL), see Fig. 1b. Its sample complexity (see SM Sec.

II) is $O(1/\varepsilon^2)$ [12]. This scheme theoretically offers an exponential advantage over EFL, making it a promising strategy for learning Pauli channels. However, achieving this advantage in practice is challenging. Errors in state preparation and measurement (SPAM) and entangling operations can increase sampling overhead and diminish the advantage. Additionally, the scheme depends on having access to perfect auxiliary qubits; errors on these qubits can bias the results and lead to incorrect parameter estimates.

In the following, we address these challenges by introducing a SPAM-robust protocol and designing an error mitigation technique specifically tailored for such learning tasks, which we refer to as error-mitigated entanglement-enhanced learning (EMEEL), see Fig. 1b and c. To mitigate errors with EMEEL, we first perform additional entanglement-free learning experiments on auxiliary qubits (AuxEFL). While both AuxEFL and EFL are entanglement-free strategies, AuxEFL is considerably simpler and more efficient because we can tailor the noise affecting the idle auxiliary qubits. We then use this information to extract the correct error-free fidelities from EEL results. Although EMEEL introduces some additional overhead due to error mitigation, it can surpass the theoretical limit of EFL when noise is weak and achieve a sampling cost that is orders of magnitude smaller. We demonstrate this enhancement through several examples involving distinguishing and characterizing Pauli channels.

III. HYPOTHESIS TESTING

We first demonstrate rigorous entanglement enhancement in Pauli channel learning through a hypothesis-testing experiment and highlight the importance of SPAM robustness. In the ideal scenario with noiseless quantum memory, this example has a provable exponential separation in sample complexity between EFL and EEL in the ideal case [24, 38], making it a rigorous benchmarking tool for our experiment. The success probability of EFL decays exponentially with system size. Consequently, if EEL experiments, which are inevitably affected by hardware noise, succeed with a higher probability, they provide evidence for entanglement enhancement in this task.

Specifically, we consider the following game between Alice and Bob of distinguishing random Pauli channels. Alice first uniformly randomly samples a Pauli P_k and a sign \pm . She then chooses one of the

following two Pauli channels with equal probability,

$$\Lambda_D(\rho) = \frac{1}{2^n} [I \text{Tr}(\rho)] , \quad (2)$$

$$\Lambda_{\pm}(\rho) = \frac{1}{2^n} \left[I \text{Tr}(\rho) \pm \frac{1}{3} P_k \text{Tr}(\rho P_k) \right] . \quad (3)$$

Denote her choice as Λ . Bob is then allowed to probe copies of Λ using a certain class of measurement schemes. After Bob's measurements are done, Alice reveals the choice of P_k (but hides the sign \pm). Bob is then challenged to guess whether $\Lambda = \Lambda_D$ or $\Lambda = \Lambda_{\pm}$ by classically post-processing the measurement data he collects. Ref. [24] shows that without utilizing entanglement with a quantum memory, Bob's average success probability for a given number of measurements M decays exponentially with system size n as (see SM Sec. II C)

$$p_s \leq \min\left(1, \frac{1}{2} + 0.43 \times M 2^{-n}\right), \quad \forall n \geq 4. \quad (4)$$

In contrast, using EEL with perfect quantum memory and entangled state preparation and measurement, Bob can correctly guess Alice's choice with a constant high probability independent of system size [12]. Concretely, Bob only needs to compute an estimator $\hat{\lambda}_k$ such that $|\hat{\lambda}_k - \lambda_k| < 1/6$ with high probability, and decides the channel was Λ_D if he obtains $|\hat{\lambda}_k| < 1/6$ and Λ_{\pm} otherwise.

In real experiments, however, SPAM errors limit EEL and cause its success probability to decay exponentially as they generally push $\hat{\lambda}_k$ to smaller values. Fortunately, there are protocols similar to randomized benchmarking [20, 28, 39, 40] that remove sensitivity to SPAM errors. These protocols isolate and amplify the fidelity of interest by repeatedly applying the channel. The fidelity can then be extracted from the decay rate of the measured Pauli expectation value as a function of the number of channel applications d . This approach is applicable to EEL as well. In this example, we use a SPAM-robust protocol with $d = 0, 1$ to calibrate away SPAM errors and demonstrate a robust entanglement enhancement (see SM Sec. II B).

We experimentally demonstrate the improved success probability of EEL compared to EFL by emulating Λ through inserting random Pauli gates, using up to 64 qubits (see SM for details of the noise injection protocol). We vary the system size from 4 to 32 qubits and compare the success probability of single-depth EEL with SPAM-robust EEL and the upper bound for EFL strategies (see Fig. 2). While single depth EEL fails to outperform EFL, the SPAM

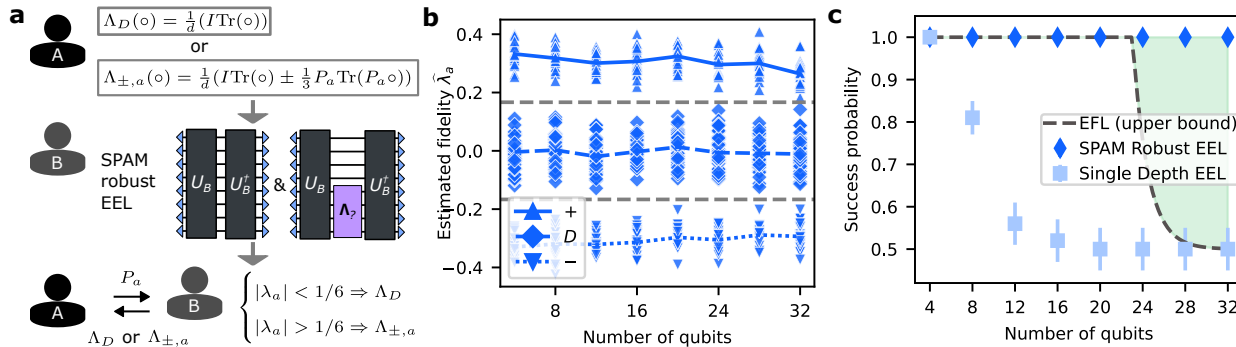


FIG. 2. **Hypothesis testing.** **a**, Schematics of the task and the SPAM robust entanglement-enhanced learning (EEL) protocol. The unitary operations U_B and U_B^\dagger correspond to state-preparation and measurement in the Bell basis between system and auxiliary qubit pairs, respectively. See Sec. III for details. **b**, Estimates for λ_a from SPAM channels, Λ_D , $\Lambda_{-,a}$, and $\Lambda_{+,a}$, in which case the true value of λ_a is 0, $-1/3$, $+1/3$, respectively. For each system size $n \in [4, 8, \dots, 32]$, we sample $a \in \mathcal{P}^n$ 50 times and plot the estimate for λ_a for each type of Pauli channel. The average over a for each type of Pauli channel is shown as solid lines. Clearly, by comparing the estimates with the thresholds $\pm 1/6$ (dash line), one can decide the type of underlying Pauli channels with high probability. **c**, Comparison of success probability in distinguishing Λ_D with $\Lambda_{\pm,a}$ via single-depth EEL, SPAM robust EEL, and entanglement-free learning (EFL) upper bound given in Eq. (4). The single-depth EEL scheme uses $M = 5 \times 10^6$ total measurements, while SPAM-robust EEL uses twice that number, $M = 5 \times 10^6$ for SPAM characterization and the same number for Pauli channel learning. While the success probability of single-depth EEL quickly converges to $1/2$ as system size increases, SPAM-robust EEL retains a success probability of almost 1 and surpasses the upper bound for EFL for $M = 10^7$ measurements, demonstrating a rigorous entanglement enhancement. The error bars and samples are obtained from random sampling of injected Pauli noise on *ibm.brisbane* (see SM).

robust protocol succeeds with overwhelming probability. Notably, for $n \geq 24$, the success probability of SPAM-robust EEL remains constant, exceeding the exponentially small upper bound for protocols without access to quantum memory, demonstrating rigorous entanglement enhancement (green shaded region in Fig. 2c). Note that because of small single-qubit gate errors and their short gate lengths errors on auxiliary qubits do not affect the results for the system sizes considered. The robustness to these small errors is due to the large margin in the decision boundary. However, we expect the success probability on noisy devices to eventually decay as system sizes grow.

IV. LEARNING NOISE IN QUANTUM OPERATIONS

Next, we move beyond emulated noise and learn real noise processes affecting gate operations in quantum processors. We model a noisy multi-qubit Clifford gate as $\tilde{\mathcal{G}} = \mathcal{G} \circ \Lambda$, where \mathcal{G} is the ideal gate and Λ is the noise process, including classical and quantum crosstalk, which is twirled into a Pauli

channel [20, 28]. The goal is to utilize entanglement to more efficiently learn the Pauli eigenvalues of Λ . Since these eigenvalues can only be characterized up to fundamentally unlearnable degrees of freedom [41], we focus on learning the symmetrized Pauli eigenvalues [2, 20, 30] (see Methods Sec. B).

The main challenge in improving sample complexity and obtaining accurate results with entanglement-enhanced schemes is the additional errors introduced by auxiliary qubits during the application of quantum gates on the system. These errors alter the fidelities extracted by EEL and bias the results. To address this, we introduce EMEEL, which incorporates an error mitigation procedure to remove this bias and recover the true fidelities.

The main idea behind EMEEL is based on the fact that when errors affecting the joint state of the system and auxiliary qubits are uncorrelated, the channel takes a tensor-product form. We use this structure to design a protocol that removes the bias introduced by auxiliary noise, at the cost of an increased variance in our EMEEL estimates, which we characterize later. In our experiments, we enforce this assumption by applying a context-aware dynamical decoupling sequence on the (idle) auxiliary qubits that removes correlated coherent errors

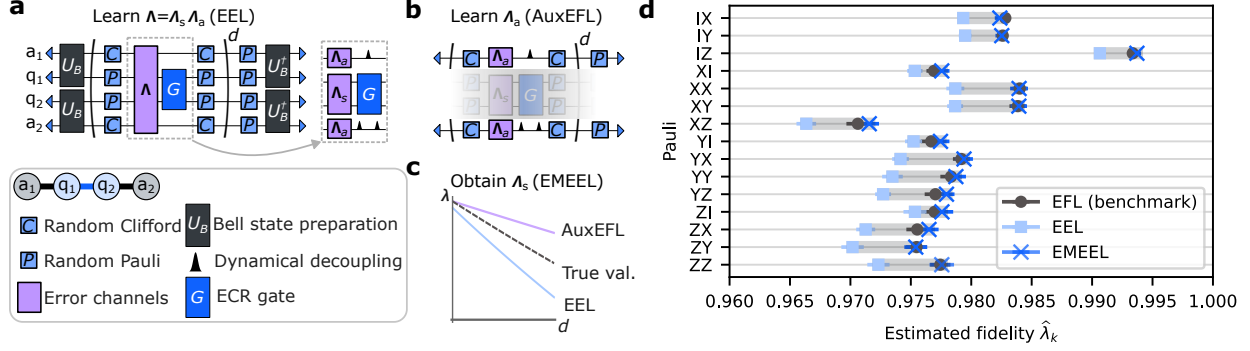


FIG. 3. **Learning the noise of a two-qubit gate.** **a**, The quantum circuit for entanglement enhanced learning of noise affecting the quantum gate G applied to qubits q_1 and q_2 , which is chosen to be an echoed cross-resonance (ECR) gate [34–37] in the experiment. The gate is applied d times interleaved by twirling layers. Here, $d = 0, 16, 32$. Auxiliary qubits a_1 and a_2 are prepared in a pairwise maximally entangled Bell state with their neighboring system qubits using U_B . The auxiliary qubits are twirled using single qubit Clifford gates (C), while the system qubits are twirled using random Pauli gates (P). In general, the error channel Λ affects all the qubits in a correlated way. However, when these errors are coherent, using a simple dynamical decoupling strategy we can decouple the error channel into $\Lambda_a \otimes \Lambda_s$, affecting the auxiliary and system qubits in an uncorrelated way, respectively. **b**, We learn Λ_a by preparing and measuring the auxiliary qubits in a fixed basis while the gate is applied to the system. Because of Clifford twirling, the Pauli fidelities of Λ_a only depend on the pattern of the Pauli string, i.e., whether a non-trivial Pauli operator acts on the qubits. **c**, The Pauli fidelities are extracted from the decay of the expectation value of the output of the circuits in panels a and b as a function of d . The EEL curve decays faster than the EFL curve. The slope of these curves determine the corresponding Pauli fidelity. When $\Lambda = \Lambda_a \otimes \Lambda_s$, the slope of EEL curve is the product of EFL and AuxEFL’s. **d**, Estimated Pauli fidelities $\hat{\lambda}_k$ of Λ_s for the 15 non-trivial Pauli (P_k) operators on two qubits. We measure the fidelities using two independent methods with and without quantum memory. We take EFL as the ground truth. Without error mitigation EEL results do not match EFL’s, with their disagreement highlighted in grey. However, after applying error mitigation we uncover correct fidelities with EMEEL. Error bars are statistical correspond to 1.96 standard deviation. The experiments were performed on *ibm_peekskill* with 100 twirls and 1000 shots at each depth.

between them and the system [42]. In these cases, it is possible to find a simple expression for the fidelities extracted by EEL.

Let \mathcal{E}' denote the Pauli noise channel acting on the auxiliary qubits with Pauli fidelities λ'_k . We find that

$$(\mathcal{E} \otimes \mathcal{E}')(|\Phi\rangle\langle\Phi|^{\otimes n}) = \sum_k \lambda_k \lambda'_k P_k \otimes P_k^T / 4^n. \quad (5)$$

Therefore, the fidelities extracted by EEL are simply scaled by their corresponding auxiliary fidelities. Consequently, we can first learn λ'_k without entanglement enhancement and then find the λ_k by simply rescaling the noisy EEL output. We refer to the former as auxiliary entanglement-free learning (AuxEFL). The combined application of EEL (Fig. 3a) and AuxEFL (Fig. 3b) followed by the post-processing step of rescaling fidelities (Fig. 3c) constitute EMEEL. Note that both the EEL fidelities and AuxEFL fidelities can be extracted using the SPAM robust technique outlined earlier.

While learning \mathcal{E}' using AuxEFL is generally as

difficult as the original EFL problem, the noise affecting idle auxiliary qubits can be simplified to a generalized depolarization channel using single-qubit Clifford twirling [43]. As a result, λ'_k depend only on the Pauli pattern, not the specific directions. This allows them to be measured simultaneously, since Pauli operators in the same basis commute (e.g., $I, Z^{\otimes n}$). Note that the same simplification using single-qubit Clifford twirling could not be done to the system due to the existence of multi-qubit gates [29]. The EMEEL protocol is explained in details in Methods Sec. B. More details on the experiments, circuits, and additional data are presented in SM Sec. VI.

A. Experimental learning of a two-qubit gate noise

We first demonstrate EMEEL by characterizing the noise of a two-qubit gate. To validate the results, we additionally perform EFL in various bases and ex-

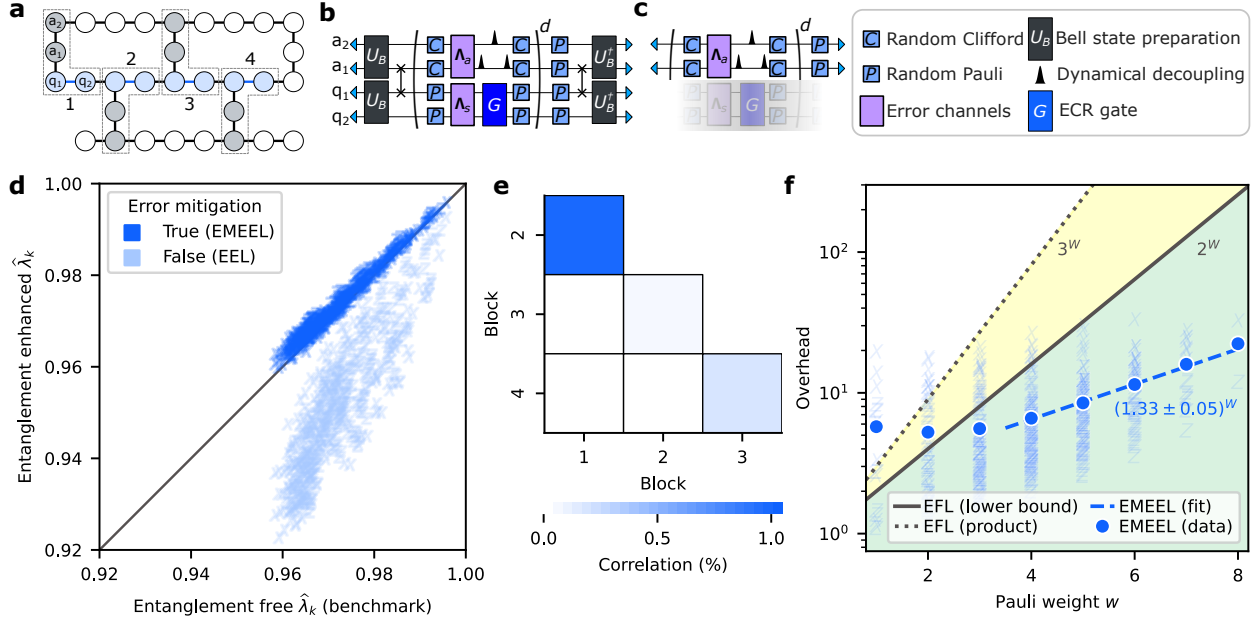


FIG. 4. **Learning noise of a layer of parallel gates.** **a**, The layout of the experiment for learning the noise channel affecting parallel gates in an 8-qubit layer (blue qubits). The layer is divided into 4 blocks of qubits (numbers along the borders). **b**, The quantum circuit for entanglement enhanced learning (EEL) of noise is similar to that of Fig. 3 for a single block in panel a. In this layout we need a SWAP operation to create a Bell state on $a_{1(2)}$ and $q_{1(2)}$. We use depths $d = 0, 16, 32$, and extract the fidelity estimates that are robust to state-preparation and measurement errors from the slope of the decay curves. **c**, Noise on auxiliary qubits, Λ_a , is learned using auxiliary entanglement-free learning protocol (AuxEFL) on those qubits. **d**, The estimated Pauli fidelities $\hat{\lambda}_k$ with EEL using quantum memory and entanglement-free learning without quantum memory (EFL) should ideally match (45 degree line) as they correspond to the same physical quantity obtained from two independent methods. However, due to the bias from auxiliary noise they do not. Error-mitigated entanglement-enhanced learning (EMEEL) restores the correct values by using information from AuxEFL to mitigate EEL estimates. While EMEEL enables access to all the Pauli fidelities, due to the prohibitive cost of EFL we only benchmark them in the X and Z basis (markers). **e**, The average correlation [see Eq. (6)] between two-qubit XX and ZZ fidelities of each pairs of blocks. The correlation between adjacent blocks indicates that errors are not local within each block. **f**, The overhead of EMEEL compared with a theoretical lower bound for EFL as a function of the Pauli weight w , i.e., the number of non-trivial qubits that the operator acts on. The lower overhead of EMEEL, $(1.33 \pm 0.05)^w$ from fit (dashed line) compared to the 2^w EFL lower bound (solid black line) and 3^w scaling of only using single qubit measurements (dotted black line) demonstrates entanglement enhancement in sample complexity. The experiments were performed on *ibm.kyiv* with 500 twirls and 500 shots at each depth.

tract all the Pauli fidelities of the noise channel (see Fig. 3d). Ideally, the Pauli fidelities from EMEEL and EFL should match, but EMEEL achieves this with only 2 measurement settings (one for EEL and one for AuxEFL), while EFL requires 9 ($\{X, Y, Z\}^{\otimes 2}$). Without error mitigation, the fidelities extracted by EEL are smaller than those from EFL with a mean absolute error of $(3.84 \pm 0.14) \times 10^{-3}$, because noise on auxiliary qubits biases the estimates towards lower values. However, by characterizing this bias with AuxEFL, EMEEL corrects for it and improves the estimation error by an order of magnitude to $(4.4 \pm 1.4) \times 10^{-4}$. The success of EMEEL also

validates the tensor product assumption and demonstrates that dynamical decoupling has effectively decoupled the system and auxiliary qubits.

B. Experimental learning of the noise on a layer of two-qubit gates

While EMEEL drastically reduces the number of measurement settings from an exponential in n for protocols without memory to 2 (one for EEL and another one for AuxEFL as shown in Fig. 3b and c), the increased variance from additional entangling gates

and auxiliary noise increase the number of times we have to measure in each setting. In the next case, we learn the noise on a parallel layer of 4 two-qubit gates on 8 qubits and answer this question about the overhead and scalability of the protocol (see Fig. 4). In SM Sec. VI we include additional results using a different layout.

We consider a configuration of parallel gates on a linear chain of qubits (Fig. 4a). This setup on the heavy-hex geometry of our quantum processor requires using SWAP gates to establish entanglement between auxiliary and system qubits (Fig. 4b). These additional gates contribute to SPAM errors, increasing the overhead of EMEEL, but do not alter the learning protocols (Fig. 4b and c).

To benchmark the accuracy of EMEEL, unlike the previous case, we cannot perform EFL for all the Pauli fidelities due to their exponential size. Instead, we measure the fidelities using EFL only in the X and Z bases and compare them with those from EMEEL (Fig. 4d). The fidelities from both methods should ideally match. Without error mitigation, EEL underestimates the fidelities due to bias introduced by auxiliary noise with a mean absolute error of $(2.081 \pm 0.004) \times 10^{-2}$. With error mitigation, EMEEL corrects this bias, improving the error by an order of magnitude to $(1.59 \pm 0.04) \times 10^{-3}$. In SM Sec. VI, we show that the small residual bias at lower fidelity values can be improved by using a different layout on the device.

Next, we characterize the correlations in noise between different qubits. Generally, geometric locality can improve the overhead of learning without quantum memory (see e.g. Refs. [2, 44, 45]). For example, if the noise on gates are completely uncorrelated, one could learn the noise affecting each gate independently and efficiently without quantum memory. However, since our entanglement enhanced protocol does not assume locality of errors on the system we can use it to probe the correlations in noise. The presence of correlations limit the applicability of protocols relying on the locality of errors. We characterize the correlation using

$$\delta_P := |\lambda_{PPPP} - \lambda_{PPII}\lambda_{IIPP}|, \quad P \in \{X, Z\}. \quad (6)$$

which quantifies the deviation of errors from a tensor product channel on two pairs of qubits. We then show the average correlation in X and Z bases, i.e., $(\delta_X + \delta_Z)/2$, in Fig. 4e. We observe correlations between adjacent pairs, but do not observe a strong correlation beyond that. We believe that the difference in the strength of correlations between adjacent pairs is related to the direction of applied

gate and the dynamical decoupling properties of the gates [34].

Finally, we compare the resource cost of EMEEL and EFL. Suppose the goal is to estimate all Pauli eigenvalues of Pauli weight up to w . Intuitively, the advantage of EMEEL is a drastic reduction of state preparation and measurement settings – only one is needed for EEL and another one for AuxEFL. In contrast, EFL protocols require at least 2^w settings using minimal stabilizer covering [28] which is experimentally challenging, or at least 3^w settings using standard Pauli measurement [20] [46]. However, EMEEL experiences an increased variance in estimating each eigenvalue due to additional SPAM noise and auxiliary QEM. Thus, for EMEEL to have an enhancement, the reduction in experimental settings must outweigh the variance overhead.

We first analytically analyze the variance overhead and then compare it with the experimental data. Under reasonable assumptions, this overhead for λ_k roughly scales as $(\alpha_k^{\text{EFL}}/\alpha_k^{\text{EEL}})^2$, where α_k is the SPAM Pauli fidelity of the corresponding protocol (see Methods Sec. C). This overhead scales exponentially with the number of qubits n when SPAM errors are uncorrelated, but should grow much slower than 2^n given a reasonable fidelity of the Bell state preparation and measurements. To estimate the overhead, we count the number of two qubit gates, measurements, and idle periods in the protocols. For EMEEL, as shown in Fig. 4b, we have the total of 5 ECR gate in state preparation (2 for Bell state preparation and 3 for SWAP). Additionally, during the SWAP operation two qubits are idle and are affected by T1 and T2 errors. The Bell measurement consists of similar operations with the additional of 4 measurements. In the corresponding EFL protocol, only measurement errors on two system qubits contribute to SPAM errors. Using the reported gate and readout fidelities together with the T1 and T2 time averaged over the qubits involved in the experiment in Table IV B), we calculate the average α_k^{EFL} and α_k^{EEL} per qubit and estimate the overhead to be 1.23 ± 0.03 . Noting that the major part of the overhead comes from the SWAP errors, we anticipate that utilizing native SWAP gates [47] can lead to further improvements.

The overhead extracted from the experimental data corroborates our theoretical prediction. Specifically, our experiments show that while the overhead grows exponentially, the base of the exponential (1.33 ± 0.05) is much smaller than the theoretical lower bound (2) and naive scaling (3) for learning without quantum memory (Fig. 4f), in agreement (within 1.25 standard deviations) with the an-

Component	Fidelity (%)
ECR	99.03 ± 0.11
T1	99.83 ± 0.02
T2	99.39 ± 0.17
Readout	99.25 ± 0.17

TABLE I. The average fidelity of operations corresponding to qubits and gates in Fig. 4. The T1 and T2 rows correspond to the fidelity of idle operation with those errors for the duration of an ECR gate.

analytically estimated overhead. These experiments demonstrate that even with noisy quantum memory, entanglement can overcome the theoretical limits on EFL sample complexity, enabling more efficient extraction of useful information about quantum processes in real experiments.

V. OUTLOOK

The slower growth of the sampling cost of EMEEL with system size compared to that of EFL demonstrates that entanglement with noisy auxiliary quantum memory considerably enhances the learning of quantum processes. This lower sampling overhead can enable quantum characterization at larger scales without requiring assumptions about locality of the errors on the system. Moreover, the prospect of learning properties of physical systems more efficiently with noisy quantum memory aided by error mitigation opens up possibilities beyond characterizing Pauli channels. For example, identifying symmetries and measuring nonlinear properties of physical systems such as entanglement entropy may also benefit from this technique.

While we did not make any assumption about the locality of noise in the system qubits, there is an implicit assumption about the locality of interactions between system and auxiliary qubits. This assumption was used in designing dynamical decoupling sequences that made EMEEL successful. This raises an interesting question about the extent of entanglement enhancement in learning quantum processes in the presence of some locality constraints.

Additionally, since SPAM errors contribute to a major part of the overhead, techniques such as heralded state preparation can be used to improve the error mitigation overhead [48]. Moreover, assessing this overhead in different quantum computing platforms, especially those with flexible qubit layout such as trapped ions [49] and neutral atoms [50] where qubit can be shuttled, may reveal interest-

ing trade-offs between the connectivity, speed, and quality of the platforms.

In the future, as we move towards realizing fault-tolerant quantum memory, it would be interesting to examine applications of (partially) error-corrected memory in learning properties of other noisy physical systems, thus bridging the gap between error-mitigated learning and error-corrected quantum metrology [51].

VI. METHODS

A. Notations and Basics

We follow the notations of Ref. [12]. Let $\mathcal{P}^n = \{I, X, Y, Z\}^{\otimes n}$ be the Pauli group modulo the global phase. The Abelian group \mathcal{P}^n is isomorphic to \mathbb{Z}_2^{2n} . In other words, each element of \mathcal{P}^n uniquely corresponds to a $2n$ -bit string

$$a = (a_x, a_z) = a_{x,1} \cdots a_{x,n} a_{z,1} \cdots a_{z,n}, \quad (7)$$

where $a_x := a_{x,1} \cdots a_{x,n}$ and $a_z := a_{z,1} \cdots a_{z,n}$ are elements of \mathbb{Z}_2^n . The corresponding Pauli operator is given by

$$P_a = \bigotimes_{j=1}^n i^{a_{x,j}a_{z,j}} X^{a_{x,j}} Z^{a_{z,j}}, \quad (8)$$

where the phase is chosen to ensure Hermiticity. Besides the standard addition and inner product defined over \mathbb{Z}_2^{2n} , we define the symplectic inner product over \mathcal{P}^n as

$$\langle a, b \rangle = \sum_{j=1}^n (a_{x,j}b_{z,j} + a_{z,j}b_{x,j}) \pmod{2}. \quad (9)$$

One can verify that $\langle a, b \rangle = 0$ if P_a and P_b commute; otherwise, $\langle a, b \rangle = 1$. In the following, we use the label a and the Pauli operator P_a interchangeably when there is no confusion. Finally, we define the *Pauli pattern* of P_a as $\text{pt}(a)$, where $\text{pt} : \mathcal{P}^n \mapsto \mathbb{Z}_2^n$ maps the i th Pauli operator to 0 if it is I and 1 otherwise. For example, $\text{pt}(XYIZI) = 11010$. The Hamming weight of $\text{pt}(a)$ is simply called the weight of P_a .

An n -qubit Pauli channel Λ is a quantum channel of the following form

$$\Lambda(\cdot) = \sum_{a \in \mathcal{P}^n} p_a P_a(\cdot) P_a, \quad (10)$$

where $\{p_a\}_a$ are the *Pauli error rates* that form a 4^n -dimensional probability distribution. An alternative expression for Λ is

$$\Lambda(\cdot) = \frac{1}{2^n} \sum_{b \in \mathcal{P}^n} \lambda_b \text{Tr}(P_b(\cdot)) P_b, \quad (11)$$

where $\{\lambda_b\}_b$ are the *Pauli eigenvalues* or *Pauli fidelities*. These two sets of parameters are related by the Walsh-Hadamard transform [28],

$$\lambda_b = \sum_{a \in \mathcal{P}^n} p_a (-1)^{\langle a, b \rangle}, \quad p_a = \frac{1}{4^n} \sum_{b \in \mathcal{P}^n} \lambda_b (-1)^{\langle a, b \rangle}. \quad (12)$$

We assume $\lambda_b > 0$ for all $b \in \mathcal{P}^n$, which should be satisfied by any reasonable gate noise channel Λ .

Let $\{|j\rangle\}_{j=0}^{2^n-1}$ denote the n -qubit computational basis. We call $|\Phi\rangle := \sum_{j=0}^{2^n-1} |jj\rangle / \sqrt{2^n}$ the (canonical) Bell state. The Bell basis $\{|\Phi\rangle_\nu\}_{\nu \in \mathcal{P}^n}$ is defined as $|\Phi\rangle_\nu := I \otimes P_\nu |\Phi\rangle$, which forms an orthonormal basis for the $2n$ -qubit Hilbert space.

B. Details of EMEEL protocol

We focus on characterizing a noisy n -qubit Clifford gate $\tilde{\mathcal{G}}$. Suppose the gate noise is Markovian and time-stationary, in which case we can model $\tilde{\mathcal{G}} = \mathcal{G} \circ \Lambda$, where \mathcal{G} is the ideal noise-free gate and Λ is the noise channel. Let $\Lambda^{\mathcal{P}}$ be the Pauli twirled version of Λ . The ideal goal is to learn the Pauli fidelities $\{\lambda_a\}_{a \in \mathcal{P}^n}$ of $\Lambda^{\mathcal{P}}$ in a SPAM-robust manner. However, it has been proven that certain Pauli fidelities cannot be identified independently from the noisy SPAM [41]. To circumvent this issue, we introduce the \mathcal{G} -symmetrized Pauli fidelity as

$$\bar{\lambda}_a := \left(\prod_{k=0}^{d_0-1} \lambda_{\mathcal{G}^k(a)} \right)^{1/d_0}, \quad \forall a \in \mathcal{P}^n. \quad (13)$$

Here d_0 is the smallest positive integer such that $\mathcal{G}^{d_0} = \mathcal{I}$. $\lambda_{\mathcal{G}^k(a)}$ denotes the fidelity corresponding to $\mathcal{G}^k(P_a)$ with a potential \pm sign ignored. As an example, the symmetrized Pauli eigenvalues for a single CNOT are listed in Table II. The symmetrized Pauli fidelity $\bar{\lambda}_a$ are SPAM-robustly learnable and has been reported in the literature [20, 30, 41, 52], thus our goal will be learning these quantities. Since EMEEL involves an auxiliary quantum memory, we recall our assumptions that the gate noise has no correlation with the ancilla noise, i.e.,

$$\widetilde{\mathcal{I} \otimes \mathcal{G}} = (\mathcal{I} \otimes \mathcal{G}) \circ (\Lambda' \otimes \Lambda). \quad (14)$$

We do allow generic SPAM noise between the system and ancilla for the Bell state preparation and Bell measurements. Finally, we make the standard assumption that single-qubit gates have negligible noise (or absorbed into the entangling gate layer).

a	$\bar{\lambda}_a$
ZI	λ_{ZI}
IX	λ_{IX}
ZX	λ_{ZX}
IZ,ZZ	$(\lambda_{IZ}\lambda_{ZZ})^{1/2}$
XI,XX	$(\lambda_{XI}\lambda_{XX})^{1/2}$
XZ,YY	$(\lambda_{XZ}\lambda_{YY})^{1/2}$
YI,YX	$(\lambda_{YI}\lambda_{YX})^{1/2}$
IY,ZY	$(\lambda_{IZ}\lambda_{ZY})^{1/2}$
XY,YZ	$(\lambda_{XY}\lambda_{YZ})^{1/2}$

TABLE II. Symmetrized Pauli eigenvalues for a single CNOT gate.

Algorithm 1 EMEEL

Input: $N_C, N_S, \mathbf{D}, N'_C, N'_S, \mathbf{D}', \mathbf{Q}$.

- 1: $\boldsymbol{\mu}^{\text{EEL}} = \text{COLLECTEEL}(N_C, N_S, \mathbf{D})$
- 2: $\mathbf{k}^{\text{AuxEFL}} = \text{COLLECTAUXEFL}(N'_C, N'_S, \mathbf{D}')$
- 3: **for** $a \in \mathbf{Q}$ **do**
- 4: $\hat{\lambda}_{\text{EEL},a} := \text{FITEEL}(\boldsymbol{\mu}^{\text{EEL}}, a)$
- 5: $\hat{\lambda}_{\text{AuxEFL},\text{pt}(a)} := \text{FITAUXEFL}(\mathbf{k}^{\text{AuxEFL}}, \text{pt}(a))$
- 6: $\hat{\lambda}_a := \hat{\lambda}_{\text{EEL},a} / \hat{\lambda}_{\text{AuxEFL},\text{pt}(a)}$
- 7: **return** $\{\hat{\lambda}_a\}_{a \in \mathbf{Q}}$.

The procedure of EMEEL is described in Algorithm 1. In the input parameters, $\mathbf{D} = [d_1, \dots, d_{|\mathcal{D}|}]$ is a list of circuit depths. We require each d_i to be an integer multiple of d_0 . See the next section for how to choose \mathbf{D} . N_C, N_S are number of random circuits per depth and number of measurement shots per circuit, respectively. The unprimed, primed version are parameters for EEL and AuxEFL, respectively; $\mathbf{Q} = [a_1, \dots, a_{|\mathbf{Q}|}] \subseteq \mathcal{P}^n$ is set of queries of Pauli fidelities. The protocol will return an estimator $\hat{\lambda}_a$ to the symmetrized Pauli fidelity $\bar{\lambda}_a$ for each $a \in \mathbf{Q}$.

The subroutines used for EMEEL are described in Algorithm 2. SAMPLEGATESEQUENCE generates a randomized gate sequence containing d layers of \mathcal{G} . Here $\{P_{a_i}\}$ are the Pauli twirling gates while $\{C_i\}$ are the local-Clifford twirling gates. The P_α and P_β are Pauli gates for measurement twirling. The identity gate will be experimentally implemented as a dynamical decoupling sequence that suppresses idling noise and system-ancilla crosstalk [42]. COLLECTEEL calls SAMPLEGATESEQUENCE as a subroutine to construct EEL experiments. Note that, $\mu_{d,i,j}$ defined in Line 14 is the ‘‘twirling-corrected’’ measurement outcome taking into account P_α, P_β . Similar for COLLECTAUXEFL. The α_x in Line 23 is the ‘‘X part’’ of the Pauli operator as defined in Eq. (7). Finally, FITEEL and FITAUXEFL extract the fidelity per layer via curve fitting to cancel the SPAM noise, as is standard for RB-type methods [28, 39, 40].

Algorithm 2 Subroutines for EMEEL

```

1: procedure SAMPLEGATESEQUENCE( $d$ )
2:   Uniformly sample  $d$  layers of single-qubit Clifford gates  $C_1, \dots, C_d$  and  $d + 2$  Pauli gates  $P_{a_1}, \dots, P_{a_d}, P_\alpha, P_\beta$ .
3:    $C_{\text{end}} := P_\alpha C_1^\dagger C_2^\dagger \dots C_d^\dagger$ .
4:    $P_{\text{end}} := P_\beta \mathcal{G}^d(P_{a_1}) \mathcal{G}^{d-1}(P_{a_2}) \dots \mathcal{G}(P_{a_d})$ .
5:   Define  $\mathcal{T}$  to be the following gate sequence
      
$$\begin{array}{ccccccc} \boxed{C_1} & \boxed{\mathcal{I}} & \boxed{C_2} & \dots & \boxed{C_d} & \boxed{\mathcal{I}} & \boxed{C_{\text{end}}} \\ \boxed{P_{a_1}} & \boxed{\mathcal{G}} & \boxed{P_{a_2}} & \dots & \boxed{P_{a_d}} & \boxed{\mathcal{G}} & \boxed{P_{\text{end}}} \end{array}$$

6:   return  $\mathcal{T}, \alpha, \beta$ 


---


8: procedure COLLECTEEL( $N_C, N_S, \mathbf{D}$ )
9:   for  $d \in \mathbf{D}$  do
10:    for  $i = 1 \dots N_C$  do
11:      $\mathcal{T}, \alpha, \beta := \text{SAMPLEGATESEQUENCE}(d)$ 
12:     for  $j = 1 \dots N_S$  do
13:      Prepare  $|\Phi\rangle$ , apply  $\mathcal{T}$ , measure in  $\{|\Phi_\nu\rangle\}$ . Denote outcome as  $\nu$ .
14:       $\mu_{d,i,j} := \nu + \alpha + \beta \in \mathbb{P}^n \cong \mathbb{Z}_2^{2n}$ .
15:     return  $\mu := \{\mu_{d,i,j}\}$ 


---


17: procedure COLLECTAUXEFL( $N_C, N_S, \mathbf{D}$ )
18:   for  $d \in \mathbf{D}$  do
19:    for  $i = 1 \dots N_C$  do
20:      $\mathcal{T}, \alpha, \beta := \text{SAMPLEGATESEQUENCE}(d)$ 
21:     for  $j = 1 \dots N_S$  do
22:      Prepare  $|0\rangle^{\otimes 2n}$ , apply  $\mathcal{T}$ , measure the ancilla in  $\{|l\rangle\}$ . Denote outcome as  $l$ .
23:       $k_{d,i,j} := l + \alpha_x \in \mathbb{Z}_2^n$ .
24:     return  $\mathbf{k} := \{k_{d,i,j}\}$ 


---


26: procedure FITEEL( $\mu, a$ )
27:   Obtain  $N_C, N_S, \mathbf{D}$  from  $\mu$ .
28:   for  $d \in \mathbf{D}$  do
29:     $\hat{f}_d := \frac{1}{N_C N_S} \sum_{i,j} (-1)^{\langle \mu, a \rangle}$ 
30:    Fit  $\{\hat{f}_d\}$  to  $f_d = \hat{\alpha}_a^{\text{EEL}} (\hat{\lambda}_a^{\text{EEL}})^d$ .
31:   return  $\hat{\lambda}_a^{\text{EEL}}$ 


---


33: procedure FITAUXEFL( $\mathbf{k}, s$ )
34:   Obtain  $N_C, N_S, \mathbf{D}$  from  $\mathbf{k}$ .
35:   for  $d \in \mathbf{D}$  do
36:     $\hat{f}_d := \frac{1}{N_C N_S} \sum_{i,j} (-1)^{k \cdot s}$ 
37:    Fit  $\{\hat{f}_d\}$  to  $f_d = \hat{\alpha}_s^{\text{AuxEFL}} (\hat{\lambda}_s^{\text{AuxEFL}})^d$ .
38:   return  $\hat{\lambda}_s^{\text{AuxEFL}}$ 


---



```

In SM Sec. III, we prove that for any a , $\hat{\lambda}_a$ given by EMEEL is a consistent (*i.e.*, asymptotically unbiased) estimator for $\bar{\lambda}_a$. For this purpose, we will show that $\hat{\lambda}_{\text{EEL},a}$ is a consistent estimator for $\bar{\lambda}_a \lambda'_{\text{pt}(a)}$, where λ'_a

denotes Pauli fidelities of the ancilla noise channel Λ' , and $\hat{\lambda}_{\text{AuxEFL},a}$ is a consistent estimator for $\lambda'_{\text{pt}(a)}$. Taking ratio of these two thus yields a consistent estimator for $\bar{\lambda}_a$.

C. Resource cost analysis

In this section, we analyze the variance overhead of EMEEL in estimating individual symmetrized Pauli eigenvalues, and compare it with the experimental setting reduction. Consider a specific $a \in \mathbb{P}^n$ with weight w . Henceforth, we omit the subscript of a or $\text{pt}(a)$ for notational conciseness. Since $\hat{\lambda}_{\text{EMEEL}} := \hat{\lambda}_{\text{EEL}} / \hat{\lambda}_{\text{AuxEFL}}$, assuming both $\hat{\lambda}_{\text{EEL}}$ and $\hat{\lambda}_{\text{AuxEFL}}$ are sufficiently close to the true values, using the first-order Taylor expansion yields,

$$\frac{\text{Var}[\hat{\lambda}_{\text{EMEEL}}]}{\text{Var}[\hat{\lambda}_{\text{EFL}}]} \approx \frac{1}{\lambda_{\text{AuxEFL}}^2} \frac{\text{Var}[\hat{\lambda}_{\text{EEL}}]}{\text{Var}[\hat{\lambda}_{\text{EFL}}]} + \frac{\lambda_{\text{EFL}}^2}{\lambda_{\text{AuxEFL}}^2} \frac{\text{Var}[\hat{\lambda}_{\text{AuxEFL}}]}{\text{Var}[\hat{\lambda}_{\text{EFL}}]}.$$
 (15)

The second term uses the assumption that $\lambda_{\text{EFL}} = \lambda_{\text{EFL}} \lambda_{\text{AuxEFL}}$, *i.e.*, the system and auxiliary noise are independent. Note that $\hat{\lambda}_{\text{EEL}}, \hat{\lambda}_{\text{AuxEFL}}, \hat{\lambda}_{\text{EFL}}$ are all obtained by fitting an exponential decay in the form of $f_{d,k} = \alpha \lambda^d$. Omitting the label of protocols for now. For simplicity, we assume each protocol only uses two circuit depths, $\{0, d\}$, in which case the fidelity estimator is given by $\hat{\lambda} := (f_d/f_0)^{1/d}$, called a ratio estimator. Indeed, let $\hat{f}_{0(d)} := f_{0(d)} + \hat{\varepsilon}_{0(d)}$,

$$\hat{\lambda} = \left(\frac{\alpha \lambda^d + \hat{\varepsilon}_d}{\alpha + \hat{\varepsilon}_0} \right)^{\frac{1}{d}} \approx \lambda \left(1 + \frac{\hat{\varepsilon}_d - \lambda^d \hat{\varepsilon}_0}{d \alpha \lambda^d} \right),$$
 (16)

up to first-order approximation in $\hat{\varepsilon}_{0(d)}$. Therefore, the variance of $\hat{\lambda}$ is given by

$$\text{Var}[\hat{\lambda}] \approx \frac{\lambda^2}{d^2 \alpha^2} \left(\text{Var}[f_0] + \text{Var}[f_d] / \lambda^{2d} \right) =: \frac{\lambda^2 V}{d^2 \alpha^2},$$
 (17)

where V is a short-hand notation for the term within the bracket. Putting this back into Eq. (15) yields,

$$\frac{\text{Var}[\hat{\lambda}_{\text{EMEEL}}]}{\text{Var}[\hat{\lambda}_{\text{EFL}}]} \approx \frac{d_{\text{EFL}}^2 \alpha_{\text{EFL}}^2 V_{\text{EEL}}}{d_{\text{EEL}}^2 \alpha_{\text{EEL}}^2 V_{\text{EFL}}} + \frac{d_{\text{EFL}}^2 \alpha_{\text{EFL}}^2 V_{\text{AuxEFL}}}{d_{\text{AuxEFL}}^2 \alpha_{\text{AuxEFL}}^2 V_{\text{EFL}}}.$$
 (18)

To proceed, we need to decide d for each protocols. One sensible choice is to let $\lambda^d \approx 1/e$, which enables a multiplicative precision estimation for λ with respect to the infidelity. There exists a procedure to efficiently search for such d [53]. Here we assume the search is done *a priori*. On the other hand, if we assume that (1) f_0 is sufficiently close to 1, so the contribution of $\text{Var}[f_0]$ to V can be ignored, and that (2) \hat{f}_d has binomial variance $\text{Var}[\hat{f}_d] = (1 - f_d)^2 / N$ (which is true if $N_S = 1$ or the noise is sufficiently uniform among different random circuit instances), then the value of V is comparable for all protocols. Finally, if we further make the assumption

that λ_{AuxEFL} is at least as large as λ_{EFL} (which means the system gate noise is at least as large as the ancilla idling noise), we have

$$\frac{\text{Var}[\hat{\lambda}_{\text{EMEEL}}]}{\text{Var}[\hat{\lambda}_{\text{EFL}}]} \approx \left(1 + \frac{r_{\text{AuxEFL}}}{r_{\text{EFL}}}\right)^2 \frac{\alpha_{\text{EFL}}^2}{\alpha_{\text{EEL}}^2} + 1. \quad (19)$$

Here $r := \ln \lambda^{-1} \approx 1 - \lambda$ when λ is close to 1. In conclusion, under all the assumptions we made in above, the variance overhead of EMEEL roughly scales as the SPAM fidelity ratio $(\alpha_{\text{EFL}}/\alpha_{\text{EEL}})^2$. Suppose each Bell pair suffers from identical and independent error, in which case $\alpha_{\text{EEL}} = c^{w/2}$ for some constant $c < 1$. As long as $c > 1/2$ (which is a mild assumption about the Bell pair fidelity), the variance overhead will grow slower than 2^w , and thus EMEEL will have an efficiency enhancement over EFL.

We remark that the above analysis only aims at understanding the rough scaling of the variance overhead rather than giving an exact prediction. In our experiments, not all assumptions made above are satisfied: For example, we choose $d = 0, 16, 32$ and extract the rate using a fit for all protocols instead of searching for individual optimal depths and using the ratio estimator. We also choose $N_S = 500$, therefore $\text{Var}[\hat{f}_d]$ does not satisfy binomial variance. Nevertheless, by directly estimating the sample variance, we obtain a variance overhead scales as 1.33^w in Fig. 4, which is considerably smaller than 2^w or 3^w , demonstrating the entanglement enhancement even in presence of noise. We also verify that, although Eq. (19) deviates from the empirical variance overhead,

Eq. (18) gives a precise prediction by inserting the empirical variance for each $\text{Var}[\hat{f}_0]$ and $\text{Var}[\hat{f}_d]$ at $d = 32$. See SM Sec. IV.

ACKNOWLEDGMENTS

We thank Elisa Bäumer for performing experiments at the beginning of this project. We thank Joseph Emerson, Luke Govia, Hsin-Yuan Huang, Abhinav Kandala, Youngseok Kim, Yunchao Liu, David McKay, Kristan Temme, Ming Yuan for helpful discussions. This research was supported in part by grant NSF PHY-2309135 to the Kavli Institute for Theoretical Physics (KITP). S.C. & L.J. acknowledge support from the ARO (W911NF-23-1-0077), ARO MURI (W911NF-21-1-0325), AFOSR MURI (FA9550-19-1-0399, FA9550-21-1-0209, FA9550-23-1-0338), NSF (OMA-1936118, ERC-1941583, OMA-2137642, OSI-2326767, CCF-2312755), NTT Research, Packard Foundation (2020-71479). A.S. and S.M. were sponsored by the Army Research Office under Grant Number W911NF-21-1-0002. The views and conclusions contained in this document are those of the authors and should not be interpreted as representing the official policies, either expressed or implied, of the Army Research Office or the U.S. Government. The U.S. Government is authorized to reproduce and distribute reprints for Government purposes notwithstanding any copyright notation herein.

-
- [1] Temme, K., Bravyi, S. & Gambetta, J. M. Error mitigation for short-depth quantum circuits. *Physical review letters* **119**, 180509 (2017).
 - [2] van Den Berg, E., Mineev, Z. K., Kandala, A. & Temme, K. Probabilistic error cancellation with sparse pauli-lindblad models on noisy quantum processors. *Nature Physics* 1–6 (2023).
 - [3] Kim, Y. *et al.* Evidence for the utility of quantum computing before fault tolerance. *Nature* **618**, 500–505 (2023).
 - [4] Lidar, D. A. & Brun, T. A. *Quantum error correction* (Cambridge university press, Cambridge, 2013).
 - [5] Degen, C. L., Reinhard, F. & Cappellaro, P. Quantum sensing. *Rev. Mod. Phys.* **89**, 035002 (2017). URL <https://link.aps.org/doi/10.1103/RevModPhys.89.035002>.
 - [6] Giovannetti, V., Lloyd, S. & Maccone, L. Quantum metrology. *Phys. Rev. Lett.* **96**, 010401 (2006). URL <https://link.aps.org/doi/10.1103/PhysRevLett.96.010401>.
 - [7] Altepeter, J. B. *et al.* Ancilla-assisted quantum process tomography. *Phys. Rev. Lett.* **90**, 193601 (2003). URL <https://link.aps.org/doi/10.1103/PhysRevLett.90.193601>.
 - [8] Mohseni, M., Reza khani, A. T. & Lidar, D. A. Quantum-process tomography: Resource analysis of different strategies. *Physical Review A* **77**, 032322 (2008).
 - [9] Xue, S. *et al.* Variational entanglement-assisted quantum process tomography with arbitrary ancillary qubits. *Phys. Rev. Lett.* **129**, 133601 (2022). URL <https://link.aps.org/doi/10.1103/PhysRevLett.129.133601>.
 - [10] D’Ariano, G. M. & Lo Presti, P. Quantum tomography for measuring experimentally the matrix elements of an arbitrary quantum operation. *Phys. Rev. Lett.* **86**, 4195–4198 (2001). URL <https://link.aps.org/doi/10.1103/PhysRevLett.86.4195>.
 - [11] Aharonov, D., Cotler, J. & Qi, X.-L. Quantum algorithmic measurement. *Nature communications* **13**, 887 (2022).
 - [12] Chen, S., Zhou, S., Seif, A. & Jiang, L. Quantum advantages for pauli channel estimation. *Physical Review A* **105**, 032435 (2022).
 - [13] Chen, S., Cotler, J., Huang, H.-Y. & Li, J. Exponential separations between learning with and with-

- out quantum memory. In *2021 IEEE 62nd Annual Symposium on Foundations of Computer Science (FOCS)*, 574–585 (IEEE, 2022).
- [14] Huang, H.-Y. *et al.* Quantum advantage in learning from experiments. *Science* **376**, 1182–1186 (2022).
- [15] Caro, M. C. Learning quantum processes and hamiltonians via the pauli transfer matrix. *ACM Transactions on Quantum Computing* **5**, 1–53 (2024).
- [16] Huelga, S. F. *et al.* Improvement of frequency standards with quantum entanglement. *Phys. Rev. Lett.* **79**, 3865–3868 (1997). URL <https://link.aps.org/doi/10.1103/PhysRevLett.79.3865>.
- [17] Escher, B., de Matos Filho, R. L. & Davidovich, L. General framework for estimating the ultimate precision limit in noisy quantum-enhanced metrology. *Nature Physics* **7**, 406–411 (2011).
- [18] Demkowicz-Dobrzański, R., Kołodyński, J. & Guţă, M. The elusive heisenberg limit in quantum-enhanced metrology. *Nature communications* **3**, 1063 (2012).
- [19] Harper, R., Flammia, S. T. & Wallman, J. J. Efficient learning of quantum noise. *Nature Physics* **16**, 1184–1188 (2020).
- [20] Erhard, A. *et al.* Characterizing large-scale quantum computers via cycle benchmarking. *Nature communications* **10**, 5347 (2019).
- [21] Ferracin, S. *et al.* Efficiently improving the performance of noisy quantum computers. *arXiv preprint arXiv:2201.10672* (2022).
- [22] Aliferis, P. & Preskill, J. Fault-tolerant quantum computation against biased noise. *Physical Review A* **78**, 052331 (2008).
- [23] Chubb, C. T. & Flammia, S. T. Statistical mechanical models for quantum codes with correlated noise. *Annales de l'Institut Henri Poincaré D* **8**, 269–321 (2021).
- [24] Chen, S., Oh, C., Zhou, S., Huang, H.-Y. & Jiang, L. Tight bounds on pauli channel learning without entanglement. *Physical Review Letters* **132**, 180805 (2024).
- [25] Chen, S. & Gong, W. Futility and utility of a few ancillas for pauli channel learning. *arXiv preprint arXiv:2309.14326* (2023).
- [26] Fawzi, O., Oufkir, A. & França, D. S. Lower bounds on learning pauli channels. *arXiv preprint arXiv:2301.09192* (2023).
- [27] Nielsen, M. A. & Chuang, I. L. *Quantum computation and quantum information* (Cambridge university press, 2010).
- [28] Flammia, S. T. & Wallman, J. J. Efficient estimation of pauli channels. *ACM Transactions on Quantum Computing* **1**, 1–32 (2020).
- [29] Wallman, J. J. & Emerson, J. Noise tailoring for scalable quantum computation via randomized compiling. *Physical Review A* **94**, 052325 (2016).
- [30] Hashim, A. *et al.* Randomized compiling for scalable quantum computing on a noisy superconducting quantum processor. *arXiv preprint arXiv:2010.00215* (2020).
- [31] Ware, M. *et al.* Experimental pauli-frame randomization on a superconducting qubit. *Phys. Rev. A* **103**, 042604 (2021). URL <https://link.aps.org/doi/10.1103/PhysRevA.103.042604>.
- [32] Choi, M.-D. Completely positive linear maps on complex matrices. *Linear algebra and its applications* **10**, 285–290 (1975).
- [33] Bennett, C. H. & Wiesner, S. J. Communication via one-and two-particle operators on einstein-podolsky-rosen states. *Physical review letters* **69**, 2881 (1992).
- [34] Sheldon, S., Magesan, E., Chow, J. M. & Gambetta, J. M. Procedure for systematically tuning up crosstalk in the cross-resonance gate. *Phys. Rev. A* **93**, 060302 (2016). URL <https://link.aps.org/doi/10.1103/PhysRevA.93.060302>.
- [35] Malekakhlagh, M., Magesan, E. & McKay, D. C. First-principles analysis of cross-resonance gate operation. *Phys. Rev. A* **102**, 042605 (2020). URL <https://link.aps.org/doi/10.1103/PhysRevA.102.042605>.
- [36] Sundaresan, N. *et al.* Reducing unitary and spectator errors in cross resonance with optimized rotary echoes. *PRX Quantum* **1**, 020318 (2020). URL <https://journals.aps.org/prxquantum/abstract/10.1103/PRXQuantum.1.020318>.
- [37] Itoko, T., Malekakhlagh, M., Kanazawa, N. & Takita, M. Three-qubit parity gate via simultaneous cross-resonance drives. *Physical Review Applied* **21**, 034018 (2024). URL <https://journals.aps.org/prapplied/abstract/10.1103/PhysRevApplied.21.034018>.
- [38] Chen, S., Zhou, S., Seif, A. & Jiang, L. Quantum advantages for pauli channel estimation. *Phys. Rev. A* **105**, 032435 (2022). URL <https://link.aps.org/doi/10.1103/PhysRevA.105.032435>.
- [39] Knill, E. *et al.* Randomized benchmarking of quantum gates. *Phys. Rev. A* **77**, 012307 (2008). URL <https://link.aps.org/doi/10.1103/PhysRevA.77.012307>.
- [40] Magesan, E., Gambetta, J. M. & Emerson, J. Scalable and robust randomized benchmarking of quantum processes. *Phys. Rev. Lett.* **106**, 180504 (2011). URL <https://link.aps.org/doi/10.1103/PhysRevLett.106.180504>.
- [41] Chen, S. *et al.* The learnability of pauli noise. *Nature Communications* **14**, 52 (2023).
- [42] Seif, A. *et al.* Suppressing correlated noise in quantum computers via context-aware compiling. In *Proceedings of the 51st Annual International Symposium on Computer Architecture* (IEEE, 2024).
- [43] Gambetta, J. M. *et al.* Characterization of addressability by simultaneous randomized benchmarking. *Phys. Rev. Lett.* **109**, 240504 (2012). URL <https://link.aps.org/doi/10.1103/PhysRevLett.109.240504>.
- [44] Shabani, A., Mohseni, M., Lloyd, S., Kosut, R. L. & Rabitz, H. Estimation of many-body quantum hamiltonians via compressive sensing. *Phys. Rev. A*

- 84, 012107 (2011). URL <https://link.aps.org/doi/10.1103/PhysRevA.84.012107>.
- [45] da Silva, M. P., Landon-Cardinal, O. & Poulin, D. Practical characterization of quantum devices without tomography. *Phys. Rev. Lett.* **107**, 210404 (2011). URL <https://link.aps.org/doi/10.1103/PhysRevLett.107.210404>.
- [46] Since we are only learning symmetrized Pauli fidelities, one might not need to go through all 3^w Pauli basis measurements. However, a lower bound of $\Omega(2^w)$ measurements is still inevitable in this setting [24].
- [47] Wei, K. X. *et al.* Native two-qubit gates in fixed-coupling, fixed-frequency transmons beyond cross-resonance interaction. *PRX Quantum* **5**, 020338 (2024). URL <https://link.aps.org/doi/10.1103/PRXQuantum.5.020338>.
- [48] Johnson, J. E. *et al.* Heralded state preparation in a superconducting qubit. *Phys. Rev. Lett.* **109**, 050506 (2012). URL <https://link.aps.org/doi/10.1103/PhysRevLett.109.050506>.
- [49] Pino, J. M. *et al.* Demonstration of the trapped-ion quantum ccd computer architecture. *Nature* **592**, 209–213 (2021).
- [50] Bluvstein, D. *et al.* Logical quantum processor based on reconfigurable atom arrays. *Nature* **626**, 58–65 (2024).
- [51] Zhou, S., Zhang, M., Preskill, J. & Jiang, L. Achieving the heisenberg limit in quantum metrology using quantum error correction. *Nature communications* **9**, 78 (2018).
- [52] Carignan-Dugas, A. *et al.* The error reconstruction and compiled calibration of quantum computing cycles. *arXiv preprint arXiv:2303.17714* (2023).
- [53] Harper, R., Hincks, I., Ferrie, C., Flammia, S. T. & Wallman, J. J. Statistical analysis of randomized benchmarking. *Physical Review A* **99**, 052350 (2019).

Entanglement enhanced learning of quantum processes at scale: Supplemental Material

Alireza Seif,^{1,*} Senrui Chen,^{2,*} Swarnadeep Majumder,¹ Haoran Liao,³ Derek S Wang,¹ Moein Malekakhlagh,¹ Ali Javadi-Abhari,¹ Liang Jiang,² and Zlatko K Mineev¹

¹*IBM Quantum, IBM T.J. Watson Research Center, Yorktown Heights, NY, USA*

²*Pritzker School of Molecular Engineering, University of Chicago, Chicago, IL, USA*

³*Department of Physics, University of California, Berkeley, CA 94720, USA*

CONTENTS

I. Pauli-transfer-matrix (PTM) representation	1
II. Pauli channel learning in black-box model	2
A. Entanglement-enhanced learning with perfect Bell pairs	2
B. Entanglement-enhanced learning with noisy Bell pairs	3
C. Hardness for entanglement-free learning from hypothesis testing	5
III. Proof for the correctness of EMEEL	6
IV. Validating formulas for EMEEL variance	9
V. Context-aware dynamical decoupling	9
VI. Experimental details and additional results	12
A. Overview of devices	12
B. Hypothesis testing	13
C. Learning noise in a single two-qubit gate	14
D. Learning noise in a layer of two-qubit gate	14
References	16

I. PAULI-TRANSFER-MATRIX (PTM) REPRESENTATION

We have defined Pauli group, Pauli channels, and Bell states in Methods Sec. A. Here we introduce the *Pauli-transfer-matrix* (PTM) representation to further simplify notations. Our notations follows, e.g., Ref. [1]. A linear operator O acting on a 2^n -dimensional Hilbert space can be viewed as a vector in a 4^n -dimensional Hilbert space. We denote this vectorization of O as $|O\rangle\rangle$ and the corresponding Hermitian conjugate as $\langle\langle O|$. The inner product within this space is the *Hilbert-Schmidt* product defined as $\langle\langle A|B\rangle\rangle := \text{Tr}(A^\dagger B)$. The *normalized Pauli operators* $\{\sigma_a := P_a/\sqrt{2^n}, a \in \mathbb{Z}_2^{2n}\}$ forms an orthonormal basis for this space. In the PTM representation, a superoperator (*i.e.*, quantum channel) becomes an operator acting on the 4^n -dimensional Hilbert space, sometimes called the Pauli transfer operator. Explicitly, we have $|\Lambda(\rho)\rangle\rangle = \Lambda^{\text{PTM}}|\rho\rangle\rangle \equiv \Lambda|\rho\rangle\rangle$, where we use the same notation to denote a channel and its Pauli transfer operator, which should be clear from the context. Specifically, a general Pauli channel Λ has the following

* These authors contributed equally to this work.

Pauli transfer operator

$$\Lambda = \sum_{a \in \mathbb{Z}_2^{2n}} \lambda_a |\sigma_a\rangle\rangle \langle\langle \sigma_a|.$$

In the PTM representation, the n -qubit Bell states are given by

$$|\Phi_v\rangle\rangle = \mathcal{P}_v \otimes \mathbf{1} |\Phi_+\rangle\rangle = \frac{1}{4^n} \sum_{u \in \mathbb{Z}_2^{2n}} (-1)^{\langle u, v \rangle} |P_u \otimes P_u^T\rangle\rangle, \quad \forall v \in \mathbb{Z}_2^{2n}, \quad (1)$$

which forms a complete basis on $\mathcal{H}_{2^{2n}}$. Also, we use $|j\rangle\rangle$ to denote the vectorization of the computational basis state $|j\rangle\langle j|$ for $j = 1 \cdots 2^n - 1$.

II. PAULI CHANNEL LEARNING IN BLACK-BOX MODEL

In this section, we review the Pauli channel learning task in the black-box model. That is, a Pauli channel Λ given as a black box for one to query. This is to be distinguished with the gate-dependent Pauli noise model that we will consider in the next section. The task we study is the following

Task 1 ((ε, δ) -Pauli eigenvalue estimation). *Given parameters $\varepsilon, \delta \in (0, 1)$, after one makes N black-box queries to an n -qubit Pauli channel Λ , a question $a \in \mathbb{P}^n$ is given and one is asked to generate an estimator $\hat{\lambda}_a$ to λ_a such that $|\lambda_a - \hat{\lambda}_a| \leq \varepsilon$ with at least $1 - \delta$ probability for any question a . N is called the sample complexity of the protocol.*

Task 1 requires estimating only one but arbitrary Pauli eigenvalue λ_a . Note that, all quantum learning procedures must complete before the choice of a is revealed, after which only classical post-processing is allowed. Importantly, this task is proved to be hard for entanglement-free learning (EFL) protocols [2] (see also Ref. [3] for a slightly more restricted class of protocols). For a constantly high success probability, this sample complexity scales as $\Omega(2^n/\varepsilon^2)$, which quickly becomes infeasible with increasing system size. In contrast, entanglement-enhanced learning (EEL) with access to perfect (noisy) quantum memory can complete this task with constant (weakly exponential) sample complexity, respectively. In the following, we first discuss EEL protocols with perfect Bell pairs, then introduce SPAM-robust EEL with noisy Bell pairs, and finally review the hardness results for EFL protocols. These are the theoretic foundations for our hypothesis testing experiment presented in the main text Sec. III.

A. Entanglement-enhanced learning with perfect Bell pairs

Let $|\phi_+\rangle = (|00\rangle + |11\rangle)/\sqrt{2}$ be one canonical Bell pair. If one applies Pauli $\{I, X, Y, Z\}$ on the first qubit and identity on the second, the output states will be the four Bell states $\{|\phi_+\rangle, |\psi_+\rangle, |\psi_-\rangle, |\phi_-\rangle\}$ where

$$|\phi_\pm\rangle = \frac{1}{\sqrt{2}}(|00\rangle \pm |11\rangle), \quad |\psi_\pm\rangle = \frac{1}{\sqrt{2}}(|01\rangle \pm |10\rangle). \quad (2)$$

Since the four Bell states form an orthogonal basis for the 2-qubit Hilbert space, a projective measurement onto that basis uniquely determines the Pauli being applied on the first qubit. This procedure is known as quantum superdense coding [4]. Generalizing this to a $2n$ -qubit system yields a Pauli channel learning scheme as follows [1]:

Let S, A be two n -qubit quantum systems. Define $|\Phi_+\rangle_{SA} := |\phi_+\rangle_{S_1 A_1} \otimes \cdots \otimes |\phi_+\rangle_{S_n A_n}$ as the canonical Bell state. It is not hard to see the density matrix of $|\Phi_+\rangle\langle\Phi_+|$ can be expressed as

$$\Phi_+ := |\Phi_+\rangle\langle\Phi_+| = \frac{1}{4^n} \sum_{a \in \mathbb{P}^n} P_a \otimes P_a^\top. \quad (3)$$

The $2n$ -qubit Bell basis is denoted by $\{|\Phi_b\rangle\}_{b \in \mathcal{P}^n}$ where $|\Phi_b\rangle := P_b \otimes I |\Phi_+\rangle$. The orthogonality between different $|\Phi_b\rangle$ can be readily checked. Alternatively,

$$\Phi_b := |\Phi_b\rangle\langle\Phi_b| = \frac{1}{4^n} \sum_{a \in \mathcal{P}^n} (-1)^{\langle a, b \rangle} P_a \otimes P_a^\top. \quad (4)$$

Consider the following experiment: Prepare $|\Phi_+\rangle_{SA}$, apply Λ on system S , then measure the whole system with the Bell basis. The probability of getting measurement outcome b is

$$\Pr[b] = \text{Tr}[\Phi_b(\Lambda_S \otimes \mathbb{1}_A(\Phi_+))] = \frac{1}{4^n} \text{Tr} \left[\Phi_b \left(\sum_{a \in \mathcal{P}^n} \lambda_a P_a \otimes P_a^\top \right) \right] = \frac{1}{4^n} \sum_{a \in \mathcal{P}^n} (-1)^{\langle a, b \rangle} \lambda_a. \quad (5)$$

Comparing this to the Walsh-Hadamard transform, one can realize that $\Pr[b]$ is exactly the Pauli error rates p of Λ . Specifically, we have

$$\lambda_a = \sum_{b \in \mathcal{P}^n} (-1)^{\langle a, b \rangle} \Pr[b]. \quad (6)$$

Now we can describe the learning protocol as follows: Repeat the above experiment N times and collect the measurement outcomes $\mathbf{b} = \{b^{(i)}\}_{i=1}^N$. Then, for any λ_a , one computes the following estimator

$$\hat{\lambda}_a[\mathbf{b}] := \frac{1}{N} \sum_{i=1}^N \hat{\lambda}_a[b^{(i)}], \quad \text{where } \hat{\lambda}_a[b] := (-1)^{\langle a, b \rangle}. \quad (7)$$

This estimator is unbiased as Eq. (6) says $\mathbb{E}_{b \sim p} (-1)^{\langle a, b \rangle} = \lambda_a$. Furthermore, the single-shot estimator is bounded between ± 1 , so Hoeffding's inequality [5] immediately gives that

$$\Pr \left[\left| \hat{\lambda}_a[\mathbf{b}] - \lambda_a \right| \geq \varepsilon \right] \leq 2 \exp \left(-\frac{1}{2} N \varepsilon^2 \right). \quad (8)$$

Therefore, this protocol estimates any λ_a to ε precision with success probability at least $1 - \delta$ using the following number of samples (i.e., queries to Λ)

$$N = 2\varepsilon^{-2} \log(2\delta^{-1}). \quad (9)$$

Crucially, this sample complexity is independent of the system size.

B. Entanglement-enhanced learning with noisy Bell pairs

In current noisy quantum computing platforms, we do not have access to perfect Bell pairs and measurement. However, with a simple calibration step, the above learning protocol can be made robust against state preparation and measurement (SPAM) error. Suppose the noisy realization of the Bell state Φ_+ and Bell measurement POVM $\{\Phi_a\}_a$ can be written as

$$\tilde{\Phi}_+ = \mathcal{E}^S(\Phi_+); \quad \tilde{\Phi}_a = (\mathcal{E}^M)^\dagger(\Phi_a), \quad (10)$$

for some CPTP maps \mathcal{E}^S , \mathcal{E}^M . We assume the ability to perform noiseless Pauli gates (or, less stringently, all Pauli gates have a gate-independent noise channel). This assumption is relevant for many existing experimental platforms and is standard for Pauli twirling-based methods [6–8]. With this assumption, one can always twirl the noise channel into a Pauli channel. In the following, we assume the Pauli twirling has been done and both \mathcal{E}^S , \mathcal{E}^M are Pauli channels. Let $\mathcal{E} := \mathcal{E}^M \circ \mathcal{E}^S$ be their composition and denote the Pauli eigenvalue of \mathcal{E} as ξ_a .

Consider the following two experiments:

1. Prepare $\tilde{\Phi}_+^{SA}$. Then measure with $\{\tilde{\Phi}_a^{SA}\}$.
2. Prepare $\tilde{\Phi}_+^{SA}$. Apply Λ on system S . Then measure with $\{\tilde{\Phi}_a^{SA}\}$.

The distribution of measurement outcome of experiment 1 can be calculated as

$$\begin{aligned}
\Pr[b]_1 &= \text{Tr}[\Phi_b(\mathcal{E}^M \circ \mathcal{E}^S)(\Phi_+)] \\
&= \frac{1}{4^n} \text{Tr} \left[\Phi_b \left(\mathcal{E} \left(\sum_{a \in \mathcal{P}^n} P_a \otimes P_a^\top \right) \right) \right] \\
&= \frac{1}{4^n} \text{Tr} \left[\Phi_b \left(\sum_{a \in \mathcal{P}^n} \xi_{a,a} P_a \otimes P_a^\top \right) \right] \\
&= \frac{1}{4^n} \sum_{a \in \mathcal{P}^n} (-1)^{\langle a,b \rangle} \xi_{a,a}.
\end{aligned} \tag{11}$$

where $\xi_{a,a}$ is the Pauli eigenvalue of \mathcal{E} corresponding to $P_a \otimes P_a$. Similarly, experiment 2 yields

$$\begin{aligned}
\Pr[b]_2 &= \text{Tr}[\Phi_b(\mathcal{E}^M \circ (\Lambda \otimes \mathbb{1}) \circ \mathcal{E}^S)(\Phi_+)] \\
&= \frac{1}{4^n} \sum_{a \in \mathcal{P}^n} (-1)^{\langle a,b \rangle} \xi_{a,a} \lambda_a,
\end{aligned} \tag{12}$$

where we use the fact that all Pauli channels commute. Compare these to Eq. (5), we see that one can use similar estimation procedure as the noiseless case to efficiently estimate $\xi_{a,a}$ and $\xi_{a,a} \lambda_a$ to small additive error with high probability from experiment 1 and 2, respectively. By dividing the latter estimator with the former, we can obtain an estimator for λ_a that is independent of $\xi_{a,a}$ in the asymptotic limit.

More formally, consider the following protocol: Repeat N_1 times experiment 1 and collect measurement outcomes $\mathbf{b} = \{b^{(i)}\}_{i=1}^{N_1}$; Then repeat N_2 times experiment 2 and collect measurement outcomes $\mathbf{c} = \{c^{(i)}\}_{i=1}^{N_2}$; Now, for any λ_a , compute the following estimators

$$\hat{\lambda}_a^{(1)} := \frac{1}{N_1} \sum_{i=1}^{N_1} (-1)^{\langle a, b^{(i)} \rangle}, \quad \hat{\lambda}_a^{(2)} := \frac{1}{N_2} \sum_{i=1}^{N_2} (-1)^{\langle a, c^{(i)} \rangle}, \quad \hat{\lambda}_a := \frac{\hat{\lambda}_a^{(2)}}{\hat{\lambda}_a^{(1)}}. \tag{13}$$

It is easy to see that $\hat{\lambda}_a$ is a consistent (*i.e.*, asymptotically unbiased) estimator for λ_a . Let us define

$$\hat{\varepsilon}_a^{(1)} := \hat{\lambda}_a^{(1)} - \xi_{a,a}, \quad \hat{\varepsilon}_a^{(2)} := \hat{\lambda}_a^{(2)} - \xi_{a,a} \lambda_a. \tag{14}$$

Thanks to the Hoeffding's inequality, if we choose

$$N_1 = 2\varepsilon_1^{-2} \log(2\delta_1^{-1}), \quad N_2 = 2\varepsilon_2^{-2} \log(2\delta_2^{-1}),$$

we have $|\hat{\varepsilon}_a^{(1)}| \leq \varepsilon_1$ with probability at least $1 - \delta_1$ and $|\hat{\varepsilon}_a^{(2)}| \leq \varepsilon_2$ with probability at least $1 - \delta_2$. Thus, the following holds with probability at least $1 - \delta_1 - \delta_2$,

$$|\hat{\lambda}_a - \lambda_a| = \left| \frac{\xi_{a,a} \lambda_a + \hat{\varepsilon}_a^{(2)}}{\xi_{a,a} + \hat{\varepsilon}_a^{(1)}} - \lambda_a \right| = \left| \frac{\hat{\varepsilon}_a^{(2)} - \lambda_a \hat{\varepsilon}_a^{(1)}}{\xi_{a,a} + \hat{\varepsilon}_a^{(1)}} \right| \leq \frac{\varepsilon_1 + \varepsilon_2}{\xi_{a,a} - \varepsilon_1}, \tag{15}$$

given that $\varepsilon_1 < \xi_{a,a}$. Now, assuming that $\xi_{a,a} \geq F$ for all a , let us substitute

$$\varepsilon_1 = \varepsilon_2 = \frac{1}{3}\varepsilon F, \quad \delta_1 = \delta_2 = \frac{1}{2}\delta. \tag{16}$$

Then, with probability no less than $1 - \delta$, one has $|\hat{\lambda}_a - \lambda_a| \leq \varepsilon$, accomplishing Task 1. The sample complexity is

$$N_1 = N_2 = 18\varepsilon^{-2} F^{-2} \log(4\delta^{-1}). \tag{17}$$

In practice, we expect the Bell state Pauli fidelity $\xi_{a,a}$ decays exponentially with the Pauli weight of a . Assume $F = f^n$ for some constant f characterizing the per qubit fidelity, the sample complexity becomes

$$N_1 = N_2 = O(f^{-2n} \varepsilon^{-2} \log \delta^{-1}), \quad (18)$$

which depends exponentially with the number of qubits n . However, as long as f is sufficiently close to 1, this sample complexity will grow mildly and is manageable for a reasonable system size. Specifically, it will have a huge separation with the sample complexity lower bound from entanglement-free schemes. We see this separation in our experiment.

C. Hardness for entanglement-free learning from hypothesis testing

In this section, we review the hardness results for learning Pauli channels with EFL protocols [2]. The proof is based on reducing learning to a hypothesis testing task. In fact, this is exactly the first task conducted in our experiment as presented in the main text Sec. III. In below, we review the hypothesis testing task and its hardness for EFL protocols.

Given $\varepsilon \leq 1/6$, define the following set of Pauli channels

$$\begin{aligned} \Lambda_{a,\pm} &= |\sigma_{\mathbf{0}}\rangle\rangle\langle\langle\sigma_{\mathbf{0}}| \pm 2\varepsilon|\sigma_a\rangle\rangle\langle\langle\sigma_a|, \quad \forall a \in \mathbb{P}^n \text{ s.t. } a \neq \mathbf{0}. \\ \Lambda_0 &= |\sigma_{\mathbf{0}}\rangle\rangle\langle\langle\sigma_{\mathbf{0}}|. \end{aligned} \quad (19)$$

In terms of Pauli error rates, it is easy to verify that

$$p_{a,\pm} = \frac{1 \pm \varepsilon(-1)^{\langle a,b \rangle}}{4^n}, \quad p_0 = \frac{1}{4^n}. \quad (20)$$

Therefore, Λ_0 is the depolarizing channel, while each $\Lambda_{a,\pm}$ can be viewed as a perturbed depolarizing channel.

Now, consider the following game: A referee randomly sample $a \in \mathbb{P}^n \setminus \{I_n\}$ and $s \in \{\pm 1\}$ from a uniform distribution. Then, he chooses one of the following two Pauli channels with equal probability: (1) $\Lambda = \Lambda_0$ or (2) $\Lambda = \Lambda_{a,s}$. A player is then allowed to query Λ using at most N shots of measurement with a specific class of learning schemes and collect classical data. After that, the referee reveal the value of a . The player is then asked to guess whether (1) $\Lambda = \Lambda_0$ or (2) $\Lambda = \Lambda_{a,s}$. He succeeds if guessing correctly. Note that, the player must finish all measurement before the revelation and can only do classical postprocessing afterwards.

Theorem 1 (Hardness for hypothesis testing with EFL [2]). *If the player uses an entanglement-free learning scheme, the average success probability is upper bounded by*

$$\Pr[\text{Success}] \leq \frac{1}{2} + 30N\varepsilon^2 \frac{2^n}{4^n - 1} = \frac{1}{2} + O(N\varepsilon^2/2^n). \quad (21)$$

Here, the average is over the choices of a , s , and the two hypotheses of Λ .

Proof. Given a, s and an entanglement-free learning scheme, use $p_0(\mathbf{o})$, $p_{a,s}(\mathbf{o})$ to denote the probability distribution over measurement outcomes under hypothesis (1), (2), respectively. Now, for a fixed a , thanks to the revelation of a 's value, the player knows the measurement distribution is either p_0 or $\mathbb{E}_{s=\pm 1} p_{a,s}$. The success probability to distinguish between these two hypotheses is upper bounded by

$$\Pr[\text{Success}|a] \leq \frac{1}{2}(1 + \text{TVD}(p_0, \mathbb{E}_s p_{a,s})). \quad (22)$$

Thus, the average success probability of distinguishing the two hypotheses is given by

$$\Pr[\text{Success}] = \mathbb{E}_a \Pr[\text{Success}|a] \leq \frac{1}{2}(1 + \mathbb{E}_a \text{TVD}(p_0, \mathbb{E}_s p_{a,s})). \quad (23)$$

On the other hand, it is shown in the proof of [2, Theorem 2] that

$$\mathbb{E}_a \text{TVD}(p_0, \mathbb{E}_s p_{a,s}) \leq 4N\varepsilon^2 \frac{2^n}{4^n - 1} \left(1 + 2\sqrt{f(2\varepsilon)}\right), \quad (24)$$

for some function f such that $f(2\varepsilon) \leq 44$ for $\varepsilon \in (0, 1/6]$. Inserting this number completes the proof. \square

By inserting $\varepsilon = 1/6$ into the above theorem and requiring $n \geq 4$, one can obtain that

$$\Pr[\text{Success}] \leq \frac{1}{2} + 0.43 \times N2^{-n}. \quad (25)$$

which gives the EFL success probability upper bound Eq. (7) in the main text.

Finally, since a learning protocol that solves Task 1 can also solve the above hypothesis testing task with success probability at least $1 - \delta$ (by simply estimating λ_a), we immediately have the following corollary:

Corollary 2. [2] *Any EFL protocols need the following number of samples to complete Task 1,*

$$N \geq \frac{1}{60}(1 - 2\delta)(2^n - 2^{-n})\varepsilon^{-2} \quad (26)$$

given that $\varepsilon \in (0, 1/6]$, $\delta \in (0, 1/2)$.

III. PROOF FOR THE CORRECTNESS OF EMEEL

In this section, we prove the EMEEL protocol, described in Methods Sec B, gives a consistent (i.e., asymptotically unbiased) estimator for each Pauli fidelity $\lambda_a^{\mathcal{G}}$. Recall that, we make the following assumptions:

1. Layers of single-qubit Clifford gates are noiseless.
2. The noises acting on the system and ancilla is time-stationary, Markovian, and have no crosstalk or contextual dependence between each other. Specifically, applying a multi-qubit Clifford gate \mathcal{G} on the system and idling the ancilla is realized as

$$\mathcal{I}^A \otimes \mathcal{G}^S \mapsto \tilde{\mathcal{I}}^A \otimes \tilde{\mathcal{G}}^S := \Lambda_{\text{anc}}^A \otimes (\Lambda_{\mathcal{G}} \circ \mathcal{G})^S$$

3. The initial state and measurement suffer from noise channel acting jointly on the system and ancilla,

$$\rho_0^{AS} \mapsto \mathcal{E}^S(\rho_0^{AS}), \quad \mathcal{M}^{AS} \mapsto (\mathcal{M} \circ \mathcal{E}^M)^{AS}.$$

The first assumption are standard [6, 7, 9, 10]. The second assumption requires the system and ancilla to be well isolated, which can be ensured via dynamical decoupling, turning off certain couplers on superconducting platforms, or moving qubits far apart on ion or atom platforms, etc. The goal is to characterize the gate noise $\Lambda_{\mathcal{G}}$ in a SPAM-robust manner. Since we are going to apply Pauli twirling, we will only be interested in learning the Pauli eigenvalue of the Pauli twirl of $\Lambda_{\mathcal{G}}$, defined as $\{\lambda_a^{\mathcal{G}}\}$. We also denote the Pauli eigenvalue of λ_{anc} as $\{\lambda_a^{\text{anc}}\}$.

As mentioned in the main text, it has been proved that not every $\lambda_a^{\mathcal{G}}$ can be learned SPAM-independently for a generic Clifford gate \mathcal{G} [9, 11], which is a fundamental limitation posted by model identifiability that is generic to any learning scheme. Take $\mathcal{G} = \text{CNOT}$ as an example, one can show that $\lambda_{XX}, \lambda_{XI}$ cannot be individually learned SPAM-independently, while their product $\lambda_{XX}\lambda_{XI}$ can be. In our work, we only focus on learning a subset of learnable degrees of freedom of $\Lambda_{\mathcal{G}}$. Formally, we aim at learning the following quantities,

Definition 1 (Symmetrized Pauli eigenvalues). *Given an n -qubit Clifford gate \mathcal{G} , let d_0 be the smallest positive integer such that $\mathcal{G}^{d_0} = \mathcal{I}$. We define the symmetrized Pauli eigenvalues as follows:*

$$\bar{\lambda}_a := \left(\prod_{k=0}^{d_0-1} \lambda_{\mathcal{G}^k(a)} \right)^{1/d_0}, \quad \forall a \in \mathbb{P}^n. \quad (27)$$

where we drop the potential \pm sign of $\mathcal{G}^k(a)$.

The task we are about to deal with is the following:

Task 2 (Gate-dependent Pauli noise estimation). *For a given multi-qubit Clifford gate \mathcal{G} , under the aforementioned assumptions, estimate the symmetrized Pauli eigenvalues $\bar{\lambda}_a^{\mathcal{G}}$ in a SPAM-robust manner.*

We remark that learning the symmetrized Pauli eigenvalues is a standard task in the literature [7, 12]. By interleaving with carefully chosen single-qubit Clifford gates, one can learn more than those symmetrized eigenvalues [8, 9, 13]. Such protocols can also be incorporated with EMEEL, but we leave such demonstration for future work. Also note that, even learning those symmetrized Pauli eigenvalues is proved to cost exponentially many measurements for EFL schemes [2, Theorem 2].

Proof of correctness for EMEEL. The protocol of EMEEL has been outlined in details at Methods Sec B. To briefly recap, it consists of two subroutines, EEL and AuxEFL, which generate an estimator for $\lambda_a^{\text{anc}} \bar{\lambda}_a$ and λ_a^{anc} , respectively. Here we assume \mathcal{G} is fixed and omit the corresponding superscript. The estimator of EMEEL is then given by the ratio of these two estimators. Therefore, we just need to show both EEL and AuxEFL give consistent estimator. This again reduces to showing the fidelity estimator at depth d is an unbiased estimator.

EEL: Use $C_j(\cdot) := C_j(\cdot)C_j^\dagger$, $\mathcal{P}_j(\cdot) := P_j(\cdot)P_j^\dagger$ to denote the corresponding unitary channel. Let us compute the probability of getting corrected measurement outcome z , averaged over random circuits at depth d ,

$$\begin{aligned} \Pr[z] &= \mathbb{E} \langle \langle \tilde{\Phi}_{z+\alpha+\beta} | \mathcal{P}_{\alpha,\beta}^{AS} \left(C_{\text{end}} \prod_{j=d}^1 \Lambda_{\text{anc}} C_j \right) \otimes \left(\mathcal{P}_{\text{end}} \prod_{j=d}^1 \Lambda_{\mathcal{G}} \mathcal{P}_j \right) | \tilde{\Phi}_+ \rangle \rangle \\ &= \langle \langle \Phi_z | \left(\mathbb{E}_{\alpha,\beta} \mathcal{P}_{\alpha,\beta} \mathcal{E}^M \mathcal{P}_{\alpha,\beta} \right)^{AS} \left(\prod_{j=d}^1 \mathbb{E}_{C_j'} \mathcal{C}_j'^\dagger \Lambda_{\text{anc}} \mathcal{C}_j \right)^A \otimes \left(\prod_{j=d}^1 \mathbb{E}_{P_j'} \mathcal{P}_j' \Lambda \mathcal{P}_j' \mathcal{G} \right)^S | \tilde{\Phi}_+ \rangle \rangle \\ &= \langle \langle \Phi_z | \sum_{a_1, a_2 \in \mathbb{P}^n} \xi_{a_1, a_2}^M \langle \sigma_{a_1, a_2} | \rangle \langle \sigma_{a_1, a_2} | \rangle^{AS} \left(\prod_{j=d}^1 \sum_{a_1 \in \mathbb{P}^n} \lambda_{\text{pt}(a_1)}^{\text{anc}} | \sigma_{a_1} \rangle \langle \sigma_{a_1} | \right)^A \otimes \left(\prod_{j=d}^1 \sum_{a_2 \in \mathbb{P}^n} \lambda_{a_2} | \sigma_{a_2} \rangle \langle \sigma_{a_2} | \mathcal{G} \right)^S | \tilde{\Phi}_+ \rangle \rangle \\ &= \frac{1}{2^n} \sum_{a \in \mathbb{P}^n} (-1)^{\langle a, z \rangle} \xi_{a, a}^M \langle \sigma_{a, a} | \rangle^{AS} \left(\sum_{a_1 \in \mathbb{P}^n} (\lambda_{\text{pt}(a_1)}^{\text{anc}})^d | \sigma_{a_1} \rangle \langle \sigma_{a_1} | \right)^A \otimes \left(\sum_{a_2 \in \mathbb{P}^n} (\lambda_{a_2} \lambda_{\mathcal{G}^\dagger(a_2)} \cdots \lambda_{\mathcal{G}^{\dagger d-1}(a_2)}) | \sigma_{a_2} \rangle \langle \sigma_{a_2} | \right)^S | \tilde{\Phi}_+ \rangle \rangle \\ &= \frac{1}{2^n} \sum_{a \in \mathbb{P}^n} (-1)^{\langle a, z \rangle} \xi_{a, a}^M (\lambda_{\text{pt}(a)}^{\text{anc}})^d \bar{\lambda}_a^d \langle \sigma_{a, a} | \tilde{\Phi}_+ \rangle \rangle \\ &= \frac{1}{4^n} \sum_{a \in \mathbb{P}^n} (-1)^{\langle a, z \rangle} \xi_{a, a}^M (\lambda_{\text{pt}(a)}^{\text{anc}})^d \bar{\lambda}_a^d \xi_{a, a}^S \\ &\equiv \frac{1}{4^n} \sum_{a \in \mathbb{P}^n} (-1)^{\langle a, z \rangle} \xi_{a, a} (\lambda_{\text{pt}(a)}^{\text{anc}})^d \bar{\lambda}_a^d. \end{aligned} \quad (28)$$

Recall that $\sigma_a = P_a / \sqrt{2^n}$ is the normalized Pauli operator, and we write $\sigma_{a_1, a_2} := \sigma_{a_1} \otimes \sigma_{a_2}$. In the second line, we use the following change of variables

$$C_j' := C_j C_{j-1} \cdots C_1, \quad P_j' := \mathcal{G}(P_j) \mathcal{G}^2(P_{j-1}) \cdots \mathcal{G}^j(P_1), \quad \forall j = 1, \dots, d, \quad (29)$$

which does not change the average thanks to the unitary invariance of the Haar measure. We also use the following fact of the noisy Bell measurement POVM

$$\begin{aligned}\langle\langle\widetilde{\Phi}_{z+\alpha+\beta}| &= \frac{1}{2^n} \sum_{a \in \mathcal{P}^n} (-1)^{\langle a, z+\alpha+\beta \rangle} \langle\langle\sigma_{a,a}|\mathcal{E}^M \\ &= \frac{1}{2^n} \sum_{a \in \mathcal{P}^n} (-1)^{\langle a, z \rangle} \langle\langle\sigma_{a,a}|\mathcal{P}_{\alpha,\beta}\mathcal{E}^M.\end{aligned}\quad (30)$$

The third line uses the property of Pauli and local Clifford twirling (see e.g. [14]). Note that Pauli twirling yields general Pauli channels, while local Clifford twirling yields Pauli channels of which the Pauli eigenvalues only depends on the pattern of the Pauli operator.

From Eq. (28) and the Walsh-Hadamard transform, we see that $\hat{f}_a(d)[z] := (-1)^{\langle z, a \rangle}$ is an unbiased estimator for $\xi_{a,a}(\lambda_{\text{pt}(a)}^{\text{anc}})^d \bar{\lambda}_a^d$, for any $a \in \mathcal{P}^n$. Thus, by picking different d , averaging the estimators over different random circuits and measurement shots, then fitting to the single exponential decay model $\hat{\xi}_{a,a}^{\text{EEL}}(\hat{\lambda}_a^{\text{EEL}})^d$, we obtain $\hat{\lambda}_a^{\text{EEL}}$ as a consistent estimator for $\lambda_{\text{pt}(a)}^{\text{anc}} \bar{\lambda}_a$.

AuxEFL: Let us compute the probability of obtaining corrected outcome z in AuxEFL, again averaged over random circuits at depth d .

$$\begin{aligned}\text{Pr}[z] &= \mathbb{E}\langle\langle\widetilde{z + \alpha_x}|\mathcal{P}_\alpha\mathcal{C}_{\text{end}}\prod_{j=d}^1\Lambda_{\text{anc}}\mathcal{C}_j|\widetilde{0}\rangle\rangle \\ &= \langle\langle z|\left(\mathbb{E}_\alpha\mathcal{P}_\alpha\mathcal{E}'^M\mathcal{P}_\alpha\right)\left(\prod_{j=d}^1\mathbb{E}_{\mathcal{C}'_j}\mathcal{C}'_j^\dagger\Lambda_{\text{anc}}\mathcal{C}'_j\right)|\widetilde{0}\rangle\rangle \\ &= \langle\langle z|\left(\sum_{a \in \mathcal{P}^n}\xi_a'^M|\sigma_a\rangle\rangle\langle\langle\sigma_a|\right)\left(\sum_{a \in \mathcal{P}^n}(\lambda_{\text{pt}(a)}^{\text{anc}})^d|\sigma_a\rangle\rangle\langle\langle\sigma_a|\right)|\widetilde{0}\rangle\rangle \\ &= \frac{1}{2^n} \sum_{\mu \in \{0,1\}^n} (-1)^{z \cdot \mu} \xi_\mu'^M \xi_\mu'^S (\lambda_\mu^{\text{anc}})^d \\ &\equiv \frac{1}{2^n} \sum_{\mu \in \{0,1\}^n} (-1)^{z \cdot \mu} \xi_\mu' (\lambda_\mu^{\text{anc}})^d\end{aligned}\quad (31)$$

In the second line we do the same change of variables as Eq. (29), and use the following fact of noisy computational basis measurement

$$\langle\langle\widetilde{z + \alpha_x}|\mathcal{E}'^M = \langle\langle z + \alpha_x|\mathcal{E}'^M = \langle\langle z|\mathcal{X}^{\alpha_x}\mathcal{Z}^{\alpha_z}\mathcal{E}'^M = \langle\langle z|\mathcal{P}_\alpha\mathcal{E}'^M, \quad (32)$$

where we can add \mathcal{Z}^{α_z} as it acts trivially on the computational basis state. (Recall α_x, α_z is the X and Z part of Pauli P_α as defined in Methods Sec A.) We also note that the SPAM noise channel here can be quite different from the EFL experiment, as very different initial state and measurement settings are applied.

Thanks to Eq. (31) and the Walsh-Hadamard transform, we see that $\hat{f}_\mu(d)[z] := (-1)^{z \cdot \mu}$ is an unbiased estimator for $\xi_\mu'(\lambda_\mu^{\text{anc}})^d$, for any $\mu \in \{0,1\}^n$. Thus, by picking different d , averaging the estimators over different random circuits and measurement shots, then fitting to the single exponential decay model $\hat{\xi}_\mu^{\text{AuxEFL}}(\hat{\lambda}_\mu^{\text{AuxEFL}})^d$, we obtain $\hat{\lambda}_\mu^{\text{AuxEFL}}$ as a consistent estimator for λ_μ^{anc} . Choosing $\mu := \text{pt}(a)$ gives us the relevant $\lambda_{\text{pt}(a)}^{\text{anc}}$. \square

IV. VALIDATING FORMULAS FOR EMEEL VARIANCE

In Methods Sec C, we obtain the following formulas for the variance overhead of EMEEL over EFL, assuming the use of ratio estimators,

$$\frac{\text{Var}[\hat{\lambda}_{\text{EMEEL}}]}{\text{Var}[\hat{\lambda}_{\text{EFL}}]} \approx \frac{d_{\text{EFL}}^2 \alpha_{\text{EFL}}^2 V_{\text{EEL}}}{d_{\text{EEL}}^2 \alpha_{\text{EEL}}^2 V_{\text{EFL}}} + \frac{d_{\text{EFL}}^2 \alpha_{\text{EFL}}^2 V_{\text{AuxEFL}}}{d_{\text{AuxEFL}}^2 \alpha_{\text{AuxEFL}}^2 V_{\text{EFL}}} \quad (33)$$

where V_{EEL} is defined as (similar for V_{AuxEFL} , V_{EFL})

$$V_{\text{EEL}} := \text{Var}[\hat{f}_0] + \text{Var}[\hat{f}_d]/\lambda_{\text{EEL}}^{2d}, \quad (34)$$

where \hat{f}_m is defined as the fidelity estimator at depth $m \in \{0, d\}$ for the corresponding protocols.

By further assuming that (1) EEL, AuxEFL, EFL all use a ratio estimator at their optimal circuit depth [15]; (2) The fidelity estimator at every depth satisfies a binomial variance; (3) The noise are sufficiently weak to allow a first-order approximation, we obtain the following formula

$$\frac{\text{Var}[\hat{\lambda}_{\text{EMEEL}}]}{\text{Var}[\hat{\lambda}_{\text{EFL}}]} \approx \left(1 + \frac{r_{\text{AuxEFL}}}{r_{\text{EFL}}}\right)^2 \frac{\alpha_{\text{EFL}}^2}{\alpha_{\text{EEL}}^2} + 1 \quad (35)$$

which roughly scales as $\alpha_{\text{EFL}}^2/\alpha_{\text{EEL}}^2$, i.e., square of the SPAM fidelity ratio.

In Fig. 4 in the main text, we calculated the overhead from experimental data by comparing the variance of the EMEEL and EFL extracted fidelities as reported by scipy’s `curve_fit` function [16]. Specifically, we examined the reported variance of the extracted EFL, AuxEFL, and EEL fidelities by fitting $f_d = \alpha\lambda^d$ (dropping the model subscript for brevity), where the variance of individual data points are supplied to the `curve_fit` function. We then calculate the variance of EMEEL by linearly expanding the variance of $\hat{\lambda}_{\text{EEL}}/\hat{\lambda}_{\text{AuxEFL}}$. We showed that the theoretically calculated overhead at optimal depth (35) captures the correct trend of the experimentally extracted overhead, but observed a difference between the exact values. We attributed those differences to the violation of assumptions (1) and (2) in deriving Eq. (35).

Here, we show that the overhead from performing the fit using only $d = 0, 32$ matches the estimated overhead using the ratio estimator in Eq. (33). In Fig. 1, we plot the overhead obtained from `curve_fit` labeled as “Realized overhead” versus predictions of Eq. (33) labeled as “Predicted overhead”. We observe that, indeed, the data falls on the 45 degree line, showing perfect agreement between the two estimates and validating Eq. (33).

V. CONTEXT-AWARE DYNAMICAL DECOUPLING

To suppress correlated errors between system and auxiliary qubits, as well as to reduce errors on the latter, we employ the context-aware dynamical decoupling (CA-DD) scheme introduced in Ref. [17]. This scheme considers the context of the circuit, including the configuration of gates and idling periods, to insert dynamical decoupling (DD) pulses.

A major source of correlated noise on the experimental systems used in this work is the static ZZ error that arises from coupling to higher levels of the transmon qubits [18–20]. The Hamiltonian of the error on a pair of qubits is given by

$$H_{11} = \frac{\nu}{2}(-I \otimes Z - Z \otimes I + Z \otimes Z), \quad (36)$$

where ν is the strength of the coupling. This type of error between arbitrary pairs of qubits can be effectively eliminated by utilizing staggered DD sequences [17, 21–24]. The simplest example of staggered pulses used to suppress this error is shown in Fig. 2a, where we apply X pulses on the idle qubits, such that the idle times between pulses are staggered. Specifically, we use $S_1 = I_{\tau/4}-X-I_{\tau/2}-X-I_{\tau/4}$ and $S_2 = I_{\tau/2}-X-I_{\tau/2}-X$,

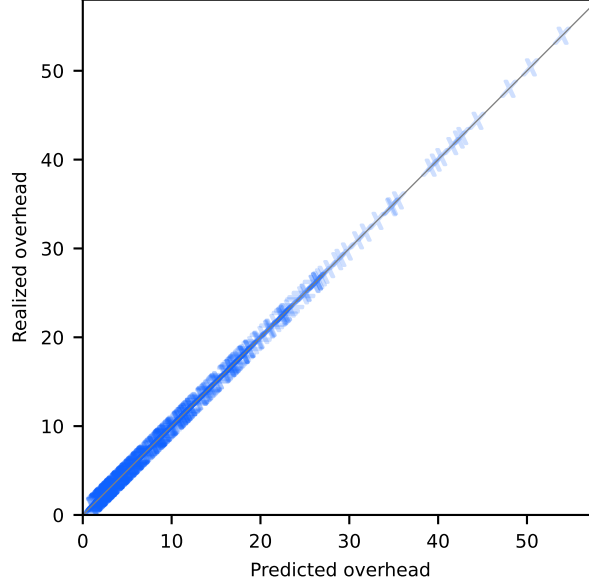


FIG. 1. **Comparison of overhead estimates.** Comparing the overhead obtained from performing the fit using only $d = 0, 32$ from the experiment in Fig. 4 in the main text with `curve_fit` labeled as “Realized overhead” versus predictions of Eq. (33) labeled as “Predicted overhead”. The data falls on the 45 degree line, showing perfect agreement between the two estimates and validating Eq. (33).

where I_t is the idle evolution for a period of t . Note that the pulses in S_2 are shifted by $\tau/4$ compared to S_1 . For a total idle period of τ , these sequences suppress the ZZ error since

$$U_\tau = e^{-i\tau/4H_{11}}.IX.e^{-i\tau/4H_{11}}.XI.e^{-i\tau/4H_{11}}.IX.e^{-i\tau/4H_{11}}.XI \quad (37)$$

$$= e^{-i\tau/4H_{11}}.e^{+i\tau/4H_{11}}.e^{-i\tau/4H_{11}}.e^{+i\tau/4H_{11}} \quad (38)$$

$$= I \quad (39)$$

The presence of gates can modify the error process, making it crucial to consider the pulses implementing the gate when applying DD. In our experiments, the native two-qubit gate, the echoed cross-resonance (ECR) gate, includes intrinsic DD pulses. These pulses must be taken into account when applying DD to idle qubits adjacent to active qubits where the gate is being applied. Specifically, the ECR gate includes an echo pulse (X) on its control qubit and two rotary echo pulses on its target qubit. Therefore, the simplest DD pulses on idle qubits that correctly stagger with the pulses on active qubits are represented by S_1 (Fig.2b) and S_2 (Fig.2c) sequences for the control and target spectators, respectively.

In this work, we focus on nearest-neighbor crosstalk errors and employ CA-DD to effectively suppress them using the fewest possible pulses. For the layouts we considered, it turns out that only two distinct pulses (S_1 and S_2) are required to suppress the crosstalk errors.

To illustrate the importance of DD, we examine the three cases mentioned above in experiments. Specifically, we perform Ramsey experiments under various scenarios and probe the coherence of qubits with different DD pulse configurations. Across all experiments, properly staggered CA-DD sequences effectively suppress both single-qubit errors and two-qubit correlated errors. In contrast, improperly selected DD pulses only address single-qubit errors and fail to suppress correlated errors.

First, we examine two idling qubits. We initialize the qubits in the $|++\rangle$ state and allow them to evolve under three distinct scenarios: (1) without DD, (2) with simple independent DD (S_1 on both qubits), and (3) with CA-DD and correct staggering (S_1 and S_2 on the qubits). We then measure p the probability of finding qubits in the $|++\rangle$ state, which should ideally remain at 1. As shown in Fig. 2a, staggered pulses yield the optimal performance, while independent DD pulses fail to fully suppress the errors.

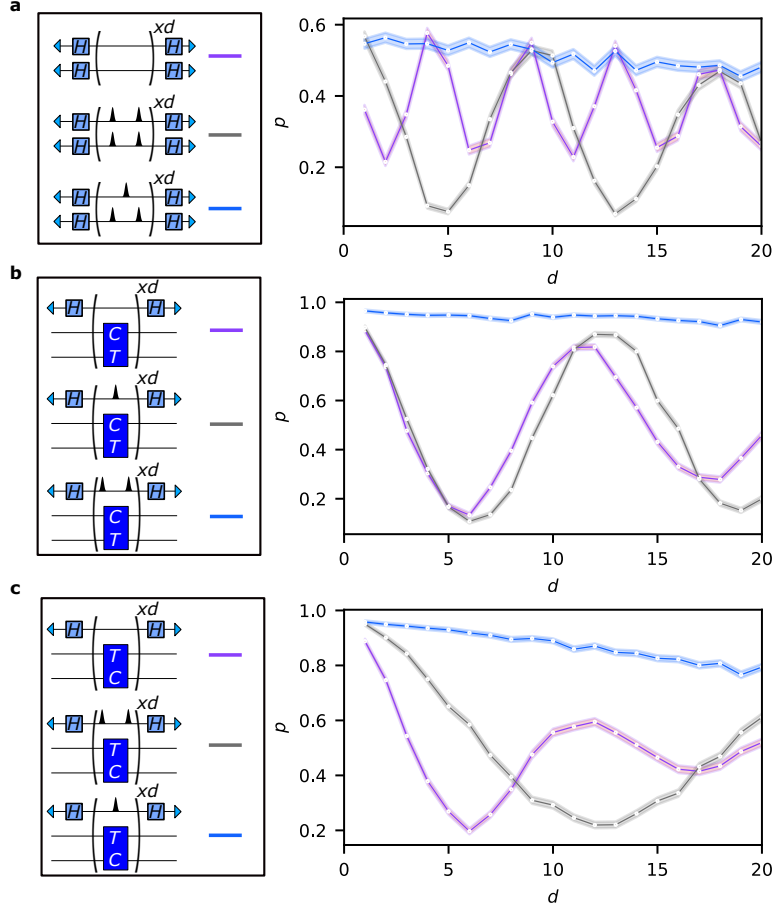


FIG. 2. Context-aware dynamical decoupling. Ramsey experiments in various contexts with different dynamical decoupling (DD) sequences. Pulse sequences are repeated d times (left panels) and the probability of return to the initial state p is measured, which should ideally remain at 1. Due to coherent errors between qubits, p oscillates. The purple curves show noisy results without any DD, the grey curves indicate context-unaware DD with aligned pulses, and the blue curves represent context-aware DD (CA-DD) with staggered pulses. In all cases, CA-DD performs the best and suppresses correlated coherent noise. **a**, Two adjacent idle qubits experiencing correlated ZZ error. Each interval is an idle period of 500 ns. **b**, The control spectator qubit, and **c**, The target spectator qubit of the echoed-cross resonance gate. The experiments are performed on *ibm_nazca* on qubits (56, 57) with 5000 shots in panel (a), on qubit 53 with the gate on qubits (60, 59) with 2000 shots in panel (b), and on qubit 53 with the gate on qubits (61, 60) with 2000 shots in panel (c).

In the second case, we focus on the control spectator and conduct single-qubit Ramsey experiments on the idle qubit while the gate is applied to its neighboring qubits. We initialize the spectator qubit in the $|+\rangle$ state and observe its evolution under three different scenarios: (1) without DD, with incorrectly aligned DD pulse (S_1), and (3) CA-DD with correct staggering in the context (S_2). We then measure the probability p of finding the qubits in the $|+\rangle$ state, which should ideally remain at 1. As illustrated in Fig. 2b, staggered pulses yield the best performance, while the application of an incorrect DD pulse fails to suppress the correlated errors.

Finally, we focus the target spectator and conduct a similar single qubit Ramsey experiment. In this case, the correctly staggered sequence is S_1 , and the incorrectly aligned sequence is S_2 . As shown in Fig. 2c, staggered pulses yield the best performance, whereas the application of an incorrect DD pulse fails to suppress the correlated errors.

We remark that in our experiments, when implementing the S_2 sequence, we exclude the final X pulse.

This exclusion is possible as the pulse can be absorbed within the twirling gates in the learning experiment.

VI. EXPERIMENTAL DETAILS AND ADDITIONAL RESULTS

In this section we present the details of experiments performed in this work. We also provide additional results concerning learning noise on gates in the experiments.

A. Overview of devices

In the characterization of a quantum processor, understanding the error properties and coherence times is important for understanding the limits and reliability of the device. The key parameters typically reported include the gate fidelity, readout error, and coherence times (T1 and T2).

Gate fidelity measures the accuracy with which our quantum gates operate. Here, we report the average gate fidelity measured through standard randomized benchmarking. For a given gate, the fidelity can then be thought of as an average over all possible input states of the fidelity between the state produced by the actual operation and the state produced by the ideal operation. For a noise channel Λ the average fidelity then is for some state $\rho_\psi = |\psi\rangle\langle\psi|$ defined over the uniform Haar average,

$$\begin{aligned} F_{\text{avg}}(\Lambda) &= \mathbb{E}_{\psi} [F(\rho_\psi, \Lambda(\rho_\psi))] \\ &= \int d\psi \langle\psi|\Lambda(|\psi\rangle\langle\psi|)|\psi\rangle \\ &= \int d\psi \langle\langle\rho_\psi|\Lambda|\rho_\psi\rangle\rangle. \end{aligned} \quad (40)$$

Readout errors indicates the probability of measurement inaccuracies. The average assignment readout error is $1 - \mathcal{F}_a$, where \mathcal{F}_a denotes the readout assignment fidelity of a qubit, defined as:

$$\mathcal{F}_a = 1 - \frac{1}{2} (P(1|0) + P(0|1)) .$$

Here, $P(A|B)$ represents the empirical probability of measuring the qubit in state $A \in \{0, 1\}$ given that it was nominally prepared in state $B \in \{0, 1\}$.

Finally, the coherence times, T1 (energy relaxation time) and T2 (phase coherence time) are the key measures of how long a qubit can maintain its quantum state before losing information.

Figures 3 and 4 depict the empirical cumulative distribution functions (CDFs) for these error probabilities and coherence times, respectively, for three IBM quantum devices: *ibm_peekskill*, *ibm_brisbane*, and *ibm_kyiv*.

Table I summarizes the error probabilities for single-qubit gates, two-qubit gates, and readout errors for the three devices. Table II provides the coherence times (T1 and T2) for the three devices.

Device	Single-Qubit Gate Error		Two-Qubit Gate Error		Readout Error	
	Mean	Median	Mean	Median	Mean	Median
<i>ibm_peekskill</i>	2.8×10^{-4}	2.3×10^{-4}	7.6×10^{-3}	7.9×10^{-3}	2.2×10^{-2}	8.5×10^{-3}
<i>ibm_brisbane</i>	4.4×10^{-4}	2.2×10^{-4}	1.0×10^{-2}	7.8×10^{-3}	2.4×10^{-2}	1.2×10^{-2}
<i>ibm_kyiv</i>	1.4×10^{-3}	3.0×10^{-4}	2.3×10^{-2}	1.2×10^{-2}	1.7×10^{-2}	6.4×10^{-3}

TABLE I. Error probabilities for single-qubit gates, two-qubit gates, and readout errors for *ibm_peekskill*, *ibm_brisbane*, and *ibm_kyiv*.

In all experiments, we utilize a fixed decomposition for the twirling gates to minimize the variations in single qubit gate errors. Specifically, we decompose the Pauli and Clifford gates required for twirling as

$$U = R_z(\alpha + \pi)\sqrt{X}R_z(\beta + \pi)\sqrt{X}R_z(\gamma), \quad (41)$$

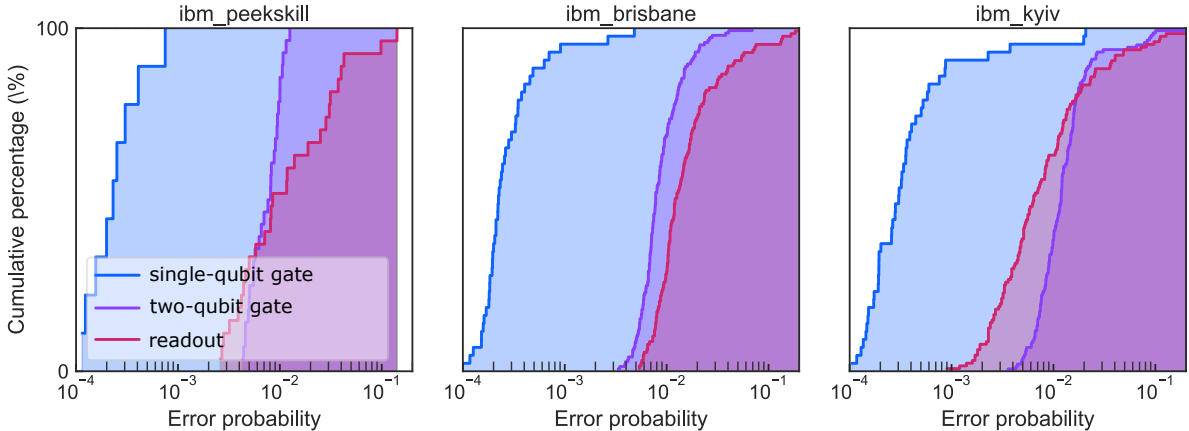


FIG. 3. Cumulative distribution functions (CDFs) for error probabilities observed in three IBM quantum devices: *ibm_peekskill*, *ibm_brisbane*, and *ibm_kyiv*. Shaded regions under the CDF curves illustrate the distribution of error probabilities across the devices. The graphs present error probabilities for single-qubit gates, two-qubit gates, and readout errors. Single-qubit gate errors refer to those of the square root of an X gate (\sqrt{X}), while two-qubit gate errors are for the native ECR gate. The x-axis depicts error probability on a logarithmic scale, and the y-axis represents the cumulative percentage of qubits or gates.

Device	T1 Time (μs)		T2 Time (μs)	
	Mean	Median	Mean	Median
<i>ibm_peekskill</i>	260	250	270	260
<i>ibm_brisbane</i>	230	240	150	140
<i>ibm_kyiv</i>	270	270	140	100

TABLE II. Coherence times (T1 and T2) for *ibm_peekskill*, *ibm_brisbane*, and *ibm_kyiv*.

where α, β, γ are the Euler angles, as shown in Figs. 5, 6, and 8.

We also employ CA-DD in all experiments except the hypothesis testing example in Fig. 2 of the main text. This ensures that the correlations between system and auxiliary qubits are suppressed. The agreement between EMEEL and EFL results further validate the success of CA-DD in suppressing such correlations.

In the following we present further details and example circuits for the experiments featured in Figs. 2, 3, and 4 in the main text and include additional results supplementing those in Figs. 3, and 4 in the main text.

B. Hypothesis testing

The first experiment concerning hypothesis testing was performed on *ibm_brisbane* using up to 64 qubits. In Fig. 5a we show the layout used in Fig. 2 in the main text. We consider system sizes $n = 4$ to 32 qubits in increments of 4. The layout for different problem sizes correspond to qubits chosen in increasing order starting from q_0 and a_0 for system and auxiliary qubits, respectively. In this example we used $d = 0$ (Fig. 5b) and $d = 1$ (Fig. 5c) to obtain a SPAM robust estimate of the fidelity of the injected noise. At each depth and size we first sample 1000 random twirls each with 10000 shots. Each random twirl at $d = 1$ is accompanied by an additional random inserted Pauli as shown in Fig. 5c.

We then use the data and the information about injected Paulis to emulate a desired Pauli channel. Specifically, in case of the depolarization channel $\Lambda_D(\hat{\rho}) = \frac{1}{2^n} [\hat{I} \text{Tr}(\hat{\rho})]$, we randomly choose 500 out of the 1000 inserted Pauli operations. Note that for a given P_k , the 500 randomly chosen Pauli operations either

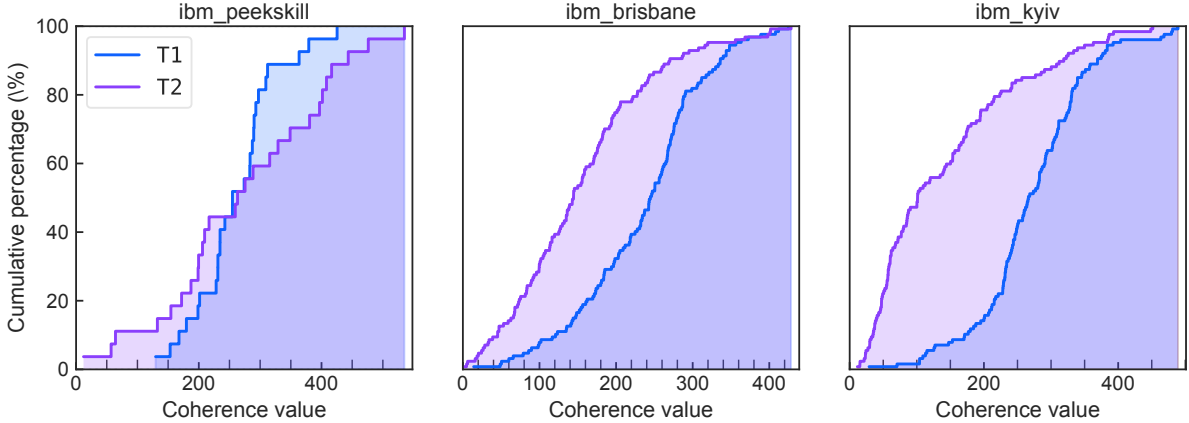


FIG. 4. Cumulative distribution functions (CDFs) of the energy relaxation T_1 and Hanh-echo coherence T_2 times for three IBM quantum devices: *ibm_peekskill*, *ibm_kyiv*, and *ibm_kyiv*. The charts illustrate the cumulative percentage of qubits exhibiting specific T_1 and T_2 coherence times. The x-axis indicates the coherence time (in μs), and the y-axis displays the cumulative percentage of qubits.

commute or anti-commute with P_k with equal probability. Therefore, on average we have $\lambda_k = 0$.

For the spiked Pauli channels $\Lambda_{\pm}(\hat{\rho}) = \frac{1}{2^n}[\hat{I} \text{Tr}(\hat{\rho}) \pm \frac{1}{3} \hat{P}_k \text{Tr}(\hat{\rho} \hat{P}_k)]$, we first choose P_k and $\lambda_k = \pm 1/3$ at random. Note that for a given λ_k , the probability of having a Pauli error that commutes with P_k is given by $p_k = (1 + \lambda_k)/2$. Therefore, we analyze the list of circuits with inserted random Paulis and label them to indicate whether the inserted Pauli operation commutes or anticommutes with P_k . We then find the number of commuting Paulis N_k according to a Binomial distribution with 500 trials and p_k , and choose N_k Paulis at random from the set of inserted Pauli operators that commute with P_k . Finally, we sample the rest of $500 - N_k$ Paulis from anticommuting ones. This procedure ensures that the emulated channels have the fidelity $\lambda_k = \pm 1/3$ on average as desired.

We repeat the above procedure 50 times for both depolarization and spiked Pauli channels to obtain the data presented in Fig. 2 in the main text.

C. Learning noise in a single two-qubit gate

The experiment concerning noise in a single two-qubit gate was performed using 4 qubits on *ibm_peekskill*. In Fig. 6a we show the layout used in Fig. 3 in the main text. In Fig. 6c, we show the circuits used for EFL (upper half) and AuxEFL (lower half). In Fig. 6d, we show the circuits used for EEL. Note that in these figures, we choose $d = 2$ to simplify the presentation. However, the data presented in Fig. 3 were obtained using $d = 0, 16, 32$ with 100 twirls, each with 1000 shots.

We also consider a different layout on *ibm_peekskill* for this example (see Fig. 6b). As shown in Fig. 7, we again observe that while EEL results deviate from the benchmark EFL results, using error mitigation EMEEL recovers the correct fidelities. Moreover, we observe that the noise on the two auxiliary qubits is very different in this experiment, resulting in a small deviations of EEL fidelity estimates from EFL's in one of the qubits, and a larger deviation in the other one.

D. Learning noise in a layer of two-qubit gate

The experiment concerning noise in a layer of 4 two-qubit gate was performed using 16 qubits on *ibm_kyiv*. In Fig. 8a we show the layout used in Fig. 4 in the main text. In Fig. 8c, we show the circuits used for EFL

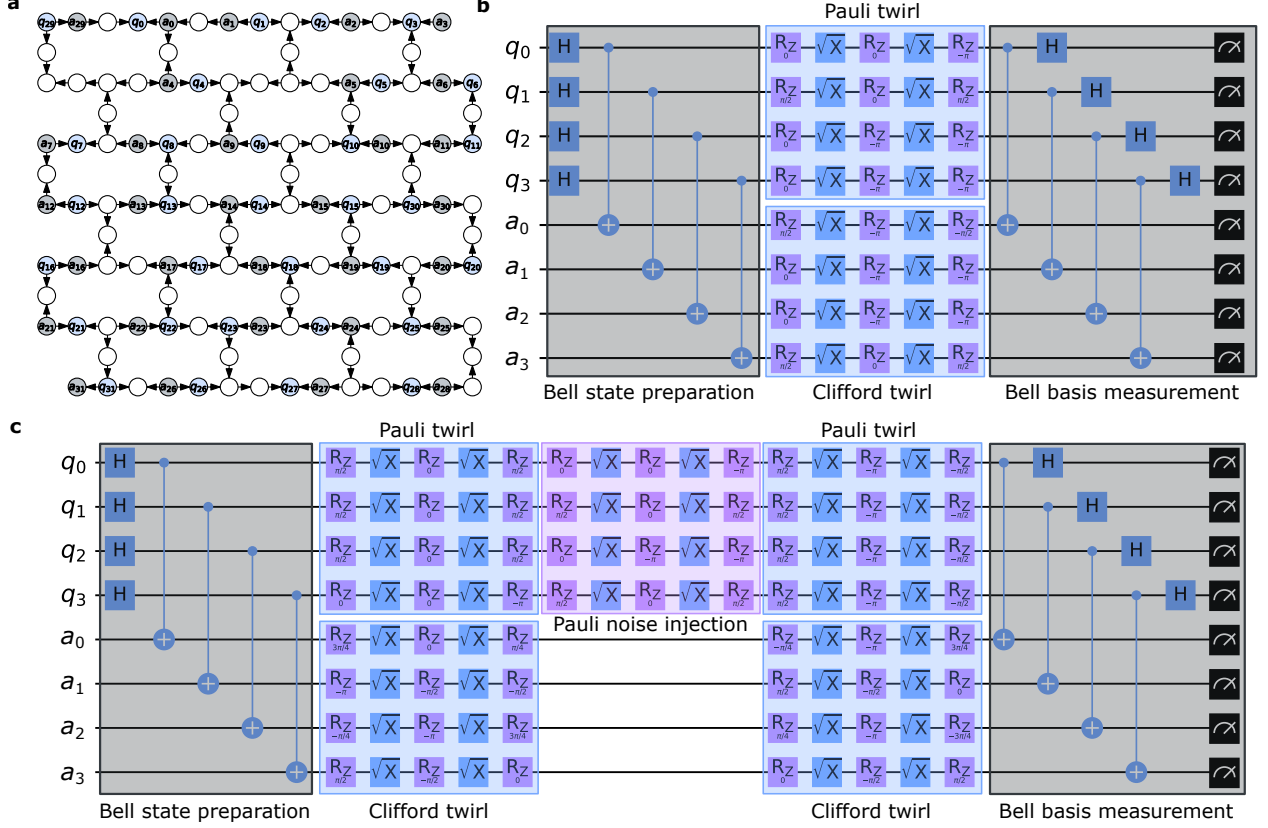


FIG. 5. **Hypothesis testing layout and circuits.** **a**, The layout used for the experiments in Fig. 2 in the main text on *ibm_brisbane*. System qubits are highlighted in blue, while auxiliary qubits are in grey. Different system sizes in Fig. 2 use qubits in this layout in increasing order. **b**, A depth-0 EEL circuit with 4 system qubits and 4 auxiliary qubits. The system qubits are Pauli twirled and auxiliary qubits are local Clifford twirled. The grey boxes indicate state preparation and measurement in the Bell basis as required by the EEL protocol. **c**, A depth-1 EEL circuit including the twirling layer and a noise injection layer. The noise is injected by randomly inserting a Pauli operator between the twirling layers.

(upper half) and AuxEFL (lower half). In Fig. 8d, we show the circuits used for EEL. Note that in these figures, we choose $d = 2$ to simplify the presentation. However, the data presented in Fig. 3 in the main text were obtained using $d = 0, 32$ with 500 twirls, each with 500 shots.

We also consider a different layout on *ibm_kyiv* for this example with two disjoint group of qubits (Fig. 8b). In this layout $\{q_0, q_1, q_2, q_3\}$ are in one group, and $\{q_4, q_5, q_6, q_7\}$ are in a different group distant from the first one. Therefore, we have 4 pair of qubits such that the first two pairs, i.e., (q_0, q_1) and (q_2, q_3) , are adjacent, and the other two pairs, i.e., (q_4, q_5) and (q_6, q_7) , are adjacent to each other and distant from the first two.

As shown in Fig. 9a, we again observe that while EEL results deviate form the benchmark EFL results, using error mitigation EMEEL recovers the correct fidelities. Moreover, we observe that the correlations are strong between adjacent pairs and almost non-existent between distant pairs (Fig. 9b). This experiment was performed with $d = 0, 32$ and 444 twirls with 500 shots each. Finally, we observe that in this layout, the overhead factor of EMEEL is $(1.18 \pm 0.02)^n$, which is much smaller than the 2^n theoretical lower bound for

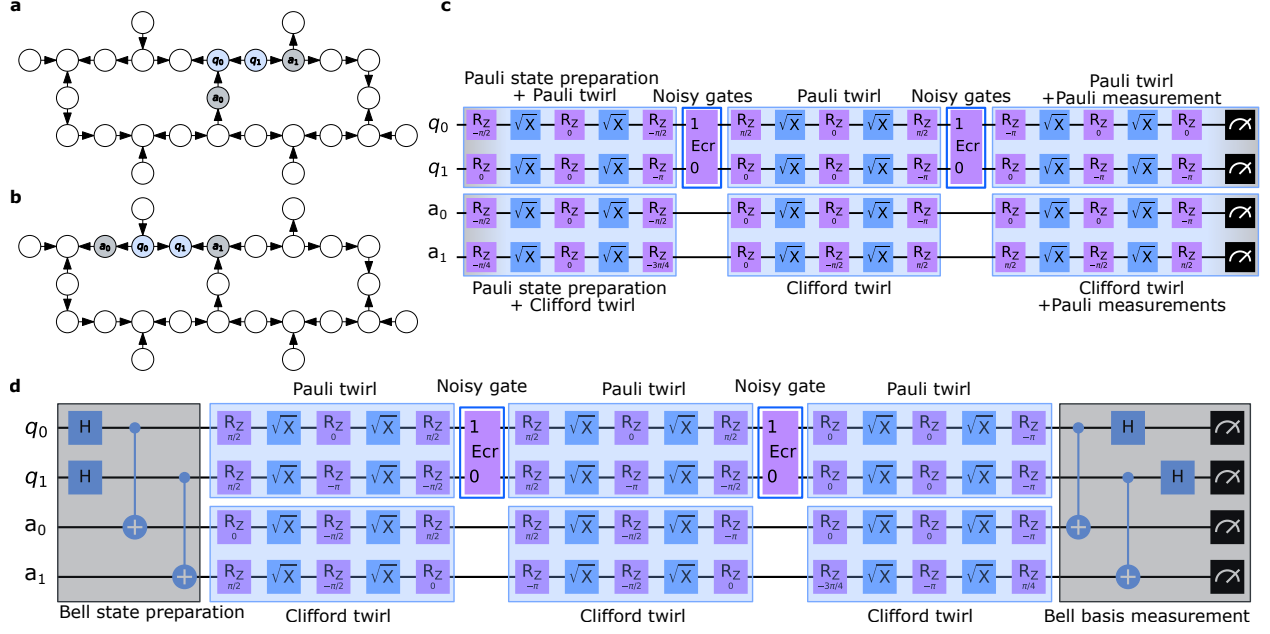


FIG. 6. **Layouts and circuits for learning noise on a two-qubit gate.** **a**, The layout used for the experiments in Fig. 3 in the main text on *ibm_peekskill*. System qubits are highlighted in blue, while auxiliary qubits are in grey. **b**, A different layout used for experiments shown in Fig. 7. **c**, A depth-2 EFL and AuxEFL circuit with 2 system qubits and 2 auxiliary qubits. The system qubits are Pauli twirled and auxiliary qubits are local Clifford twirled. The noisy echoed-cross resonance (ECR) gate is applied to the system. The state-preparation and measurement operations only require single-qubit gates, which are combined with the twirling layers. **d**, A depth-2 EEL circuit. The grey boxes indicate state preparation and measurement in the Bell basis as required by the EEL protocol. The twirling layers and noisy gate layers are similar to the previous panel.

EFL.

-
- [1] Chen, S., Zhou, S., Seif, A. & Jiang, L. Quantum advantages for pauli channel estimation. *Physical Review A* **105**, 032435 (2022).
 - [2] Chen, S., Oh, C., Zhou, S., Huang, H.-Y. & Jiang, L. Tight bounds on pauli channel learning without entanglement. *Physical Review Letters* **132**, 180805 (2024).
 - [3] Chen, S. & Gong, W. Futility and utility of a few ancillas for pauli channel learning. *arXiv preprint arXiv:2309.14326* (2023).
 - [4] Bennett, C. H. & Wiesner, S. J. Communication via one-and two-particle operators on einstein-podolsky-rosen states. *Physical review letters* **69**, 2881 (1992).
 - [5] Hoeffding, W. Probability inequalities for sums of bounded random variables. *The collected works of Wassily Hoeffding* 409–426 (1994).
 - [6] Wallman, J. J. & Emerson, J. Noise tailoring for scalable quantum computation via randomized compiling. *Physical Review A* **94**, 052325 (2016).
 - [7] Hashim, A. *et al.* Randomized compiling for scalable quantum computing on a noisy superconducting quantum processor. *arXiv preprint arXiv:2010.00215* (2020).
 - [8] van Den Berg, E., Mineev, Z. K., Kandala, A. & Temme, K. Probabilistic error cancellation with sparse pauli-lindblad models on noisy quantum processors. *Nature Physics* 1–6 (2023).
 - [9] Chen, S. *et al.* The learnability of pauli noise. *Nature Communications* **14**, 52 (2023).
 - [10] Flammia, S. T. & Wallman, J. J. Efficient estimation of pauli channels. *ACM Transactions on Quantum Computing* **1**, 1–32 (2020).
 - [11] Huang, H.-Y., Flammia, S. T. & Preskill, J. Foundations for learning from noisy quantum experiments. *arXiv*

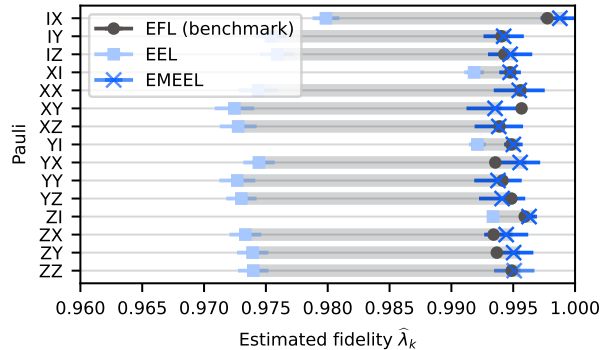


FIG. 7. **Learning noise on a two-qubit gate.** Estimated Pauli fidelities $\hat{\lambda}_k$ of Λ_s for the 15 non-trivial Pauli (P_k) operators on the two qubit depicted in Fig. 6b on *ibm_peekskill*. Similar to Fig. 3 in the main text, we measure the fidelities using two independent methods with and without quantum memory. We take EFL as the ground truth. Without error mitigation EEL results do not match EFL's, with their disagreement highlighted in grey. However, after applying error mitigation we uncover correct fidelities with EMEEL. In this layout one the auxiliary qubits have a much better fidelity than the other one as demonstrated by the difference between the single-qubit EEL fidelities. Error bars are statistical correspond to 1.96 standard deviation.

preprint *arXiv:2204.13691* (2022).

- [12] Erhard, A. *et al.* Characterizing large-scale quantum computers via cycle benchmarking. *Nature communications* **10**, 5347 (2019).
- [13] van den Berg, E. & Wocjan, P. Techniques for learning sparse pauli-lindblad noise models. *arXiv preprint arXiv:2311.15408* (2023).
- [14] Gambetta, J. M. *et al.* Characterization of addressability by simultaneous randomized benchmarking. *Phys. Rev. Lett.* **109**, 240504 (2012). URL <https://link.aps.org/doi/10.1103/PhysRevLett.109.240504>.
- [15] Harper, R., Hincks, I., Ferrie, C., Flammia, S. T. & Wallman, J. J. Statistical analysis of randomized benchmarking. *Physical Review A* **99**, 052350 (2019).
- [16] Virtanen, P. *et al.* SciPy 1.0: Fundamental Algorithms for Scientific Computing in Python. *Nature Methods* **17**, 261–272 (2020).
- [17] Seif, A. *et al.* Suppressing correlated noise in quantum computers via context-aware compiling. In *Proceedings of the 51st Annual International Symposium on Computer Architecture* (IEEE, 2024).
- [18] Tripathi, V., Khezri, M. & Korotkov, A. N. Operation and intrinsic error budget of a two-qubit cross-resonance gate. *Phys. Rev. A* **100**, 012301 (2019). URL <https://link.aps.org/doi/10.1103/PhysRevA.100.012301>.
- [19] Magesan, E. & Gambetta, J. M. Effective hamiltonian models of the cross-resonance gate. *Phys. Rev. A* **101**, 052308 (2020). URL <https://link.aps.org/doi/10.1103/PhysRevA.101.052308>.
- [20] Malekakhlagh, M., Magesan, E. & McKay, D. C. First-principles analysis of cross-resonance gate operation. *Phys. Rev. A* **102**, 042605 (2020). URL <https://link.aps.org/doi/10.1103/PhysRevA.102.042605>.
- [21] Leung, D. Simulation and reversal of n-qubit hamiltonians using hadamard matrices. *Journal of Modern Optics* **49**, 1199–1217 (2002).
- [22] Rotteler, M. & Wocjan, P. Equivalence of decoupling schemes and orthogonal arrays. *IEEE transactions on information theory* **52**, 4171–4181 (2006).
- [23] Zhou, Z., Sitler, R., Oda, Y., Schultz, K. & Quiroz, G. Quantum crosstalk robust quantum control. *Phys. Rev. Lett.* **131**, 210802 (2023). URL <https://link.aps.org/doi/10.1103/PhysRevLett.131.210802>.
- [24] Shirizly, L., Misguich, G. & Landa, H. Dissipative dynamics of graph-state stabilizers with superconducting qubits. *Phys. Rev. Lett.* **132**, 010601 (2024). URL <https://link.aps.org/doi/10.1103/PhysRevLett.132.010601>.

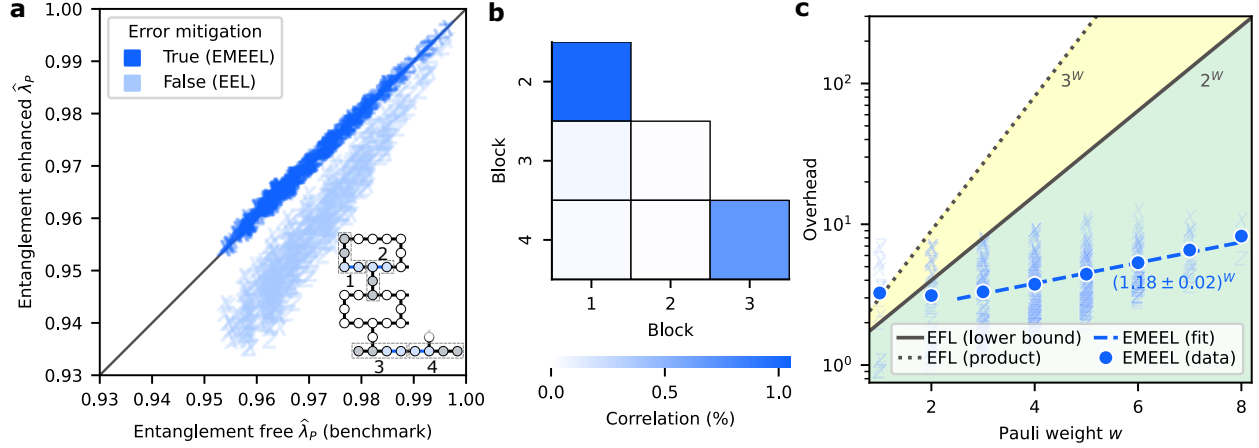


FIG. 9. **Learning noise in a layer of parallel gates.** Similar to the experiment depicted in Fig.4 of the main text, but conducted on a distinct layout featuring two distant groups of qubits, as illustrated in Fig.8b. **a**, The estimated Pauli fidelities $\hat{\lambda}_P$ using entanglement enhancement with quantum memory (EEL) and entanglement-free learning without quantum memory (EFL) should ideally align with the 45-degree line, as they correspond to the same physical quantity derived from two independent methods. However, due to bias from auxiliary noise, they do not. Error-mitigated entanglement-enhanced learning (EMEEL) restores the correct values by using information from AuxEFL to mitigate errors in EEL estimates. In principle, EMEEL enables access to all the Pauli fidelities, however, due to the prohibitive cost of EFL we only benchmark them in the X and Z basis (markers). The inset shows the layout. **b**, The average correlation between two-qubit XX and ZZ fidelities of each pair of blocks. Adjacent pairs exhibit strong correlation (1,2) and (3,4), whereas distant pairs show negligible correlations. The block index $i+1$ corresponds to qubit pairs as shown in the inset of panel a. **c**, The overhead of EMEEL compared with a theoretical lower bound for EFL as a function of the Pauli weight w , i.e., the number of non-trivial qubits that the operator acts on. The lower overhead of EMEEL, $(1.18 \pm 0.02)^w$ from fit, compared to the 2^w theoretical lower bound for EFL and the 3^w overhead for single-qubit measurements demonstrate entanglement enhancement in sample complexity.